AGU PUBLICATIONS

JGR

Journal of Geophysical Research: Oceans

RESEARCH ARTICLE

10.1002/2015JC011117

Ice shelf basal melt rates around Antarctica from simulations and observations

M. P. Schodlok[1,2], D. Menemenlis[2], and E. J. Rignot[2,3]

[1]Joint Institute for Regional Earth System Science and Engineering, University of California Los Angeles, Los Angeles, California, USA, [2]Jet Propulsion Laboratory, California Institute of Technology, Pasadena, California, USA, [3]Department of Earth System Science, University of California Irvine, Irvine, California, USA

Key Points:
- Explicit representation of ice-shelf-ocean interaction in an ocean reanalysis
- Compare modeled basal melt rates and pattern to estimates derived from satellite data
- Evaluate sources of error in explicit representation of ice shelf ocean interaction

Correspondence to:
M. P. Schodlok,
schodlok@jpl.nasa.gov

Citation:
Schodlok, M. P., D. Menemenlis, and E. J. Rignot (2016), Ice shelf basal melt rates around Antarctica from simulations and observations, *J. Geophys. Res. Oceans*, *121*, 1085–1109, doi:10.1002/2015JC011117.

Received 8 JUL 2015
Accepted 21 DEC 2015
Accepted article online 26 DEC 2015
Published online 3 FEB 2016

Abstract We introduce an explicit representation of Antarctic ice shelf cavities in the Estimating the Circulation and Climate of the Ocean, Phase II (ECCO2) ocean retrospective analysis; and compare resulting basal melt rates and patterns to independent estimates from satellite observations. Two simulations are carried out: the first is based on the original ECCO2 vertical discretization; the second has higher vertical resolution particularly at the depth range of ice shelf cavities. The original ECCO2 vertical discretization produces higher than observed melt rates and leads to a misrepresentation of Southern Ocean water mass properties and transports. In general, thicker levels at the base of the ice shelves lead to increased melting because of their larger heat capacity. This strengthens horizontal gradients and circulation within and outside the cavities and, in turn, warm water transports from the shelf break to the ice shelves. The simulation with more vertical levels produces basal melt rates (1735 $\pm$ 164 Gt/a) and patterns that are in better agreement with observations. Thinner levels in the sub-ice-shelf cavities improve the representation of a fresh/cold layer at the ice shelf base and of warm/salty water near the bottom, leading to a sharper pycnocline and reduced vertical mixing underneath the ice shelf. Improved water column properties lead to more accurate melt rates and patterns, especially for melt/freeze patterns under large cold-water ice shelves. At the 18 km grid spacing of the ECCO2 model configuration, the smaller, warm-water ice shelves cannot be properly represented, with higher than observed melt rates in both simulations.

1. Introduction

The Antarctic Ice Sheet loses mass through iceberg calving at the ice shelf front and basal melt at the base of the ice shelves. The latter is a larger contribution by ~20% [*Rignot et al*., 2013] and has a larger impact on local water mass formation. On the one hand, ice shelves, which comprise about 45% of the Antarctic coastline, provide heat and freshwater fluxes through basal melt at the ice-shelf-ocean interface, transforming water masses in the sub-ice-shelf cavity and on the continental shelf. These water masses subsequently constitute an important part of deep and bottom water mass formation on the southern continental shelf and beyond [*Foldvik et al*., 1985; *Hellmer et al*., 2005; *Schodlok et al*., 2008]. Icebergs, on the other hand, float away from their region of calving and provide heat and freshwater fluxes farther away from the ice shelf, constituting local sources for, e.g., bio-productivity [*Smith et al*., 2007], but not contributing to water mass formation near the ice-shelf-ocean interface. One exception is when icebergs become grounded, in which case they can impact continental shelf circulation with consequences to exchanges between continental shelf and ice-shelf cavity water masses [*Grosfeld et al*., 2001], hence changing ice-shelf-ocean heat and freshwater fluxes and the ice-shelf mass balance.

Previous studies [e.g., *Gille*, 2002; *Jacobs*, 2006; *Schmidtko et al*., 2014] have reported significant recent changes in Southern Ocean water masses. The general trends are toward increased temperature and decreased salinity, which might cause or result from increasing Antarctic Ice Sheet mass loss, changes in precipitation, sea ice formation, wind regime and associated changes in ocean and atmosphere circulation. To quantify the ocean contribution to the mass loss of the Antarctic ice sheet, we need to investigate and understand the mechanisms of heat and freshwater fluxes between the open ocean and the ice shelf cavities and the impact of these fluxes on basal melt patterns and rates. Improved quantification and understanding of ice-shelf-ocean interaction will enable better description and prediction of the impact of ice shelves on ice sheet mass balance and global sea level change. Changes in ice shelf thickness and

grounding line position affect the stability and flow speed of outlet glaciers that nourish them with ice from the continent. Improved representation of ice shelves and of their interaction with the ocean is therefore also critical to study the stability of the Antarctic Ice Sheet and its current and future contribution to sea level rise [e.g., *Thomas and Bentley*, 1978].

Estimates of basal melt are currently derived from ocean heat content analyses [e.g., *Jacobs et al*., 2011], satellite data [e.g., *Joughin and Padman*, 2003; *Rignot et al*., 2013; *Paolo et al*., 2015], noble gases or stable isotopes and CFC's [*Loose et al*., 2009], and sparse measurements [e.g., *Stanton et al*., 2013]. In situ observations of basal freezing and melting rates, spatial patterns, and temporal variability for the majority of the ice shelves are nonexistent or scarce. Hence, most numerical simulations are poorly constrained or unconstrained by observations. Modeling ice-shelf-ocean interaction in global or Antarctic circumpolar configurations dates back to *Beckmann et al*. [1999] who used a steady-state approach, whereby the ice shelf is a rigid slab without flexural response and all basal retreat is compensated with a northward advance of glacier ice. Most model studies since then, including the present study, have followed this steady state approach. Circumpolar numerical simulations estimate basal melt rates ranging from 900 Gt/a when only the larger well documented ice shelves are included [*Hellmer*, 2004] to 1600 Gt/a when a more complete set of ice shelves is included [*Timmermann et al*., 2012]. Higher-resolution regional models focused, among others, on the Antarctic Peninsula [*Holland et al*., 2010; *Dinniman et al*., 2012], Amundsen-Bellingshausen Sea [*Schodlok et al*., 2012], and Sabrina Coast [*Khazendar et al*., 2013], and may be used to assess the circumpolar/global model estimates.

Ice-shelf-ocean interactions are not represented in current-generation models used for climate change projections (IPCC AR5) [*Stocker et al*., 2013]. Ice-shelf-ocean interactions are also not represented in current-generation global-ocean retrospective analyses [e.g., *Xue et al*., 2012; *Wunsch and Heimbach*, 2013]. A key motivation and objective of the present study is to explore the impact of including an explicit representation of ice-shelf-ocean interaction in a state-of-the-art ocean reanalysis, and by extension in the oceanic components of IPCC-class climate simulations.

Specifically, we evaluate the impact of incorporating an explicit representation of ice-shelf-ocean interaction in the Estimating the Circulation and Climate of the Ocean, Phase II (ECCO2) [*Menemenlis et al*., 2008] ocean model configuration. A recent study by *Dotto et al*. [2014] showed that one of the ECCO2 solutions had trouble reproducing observed water masses in the Weddell Sea, a limitation that we investigate in this study. The missing fresh water fluxes from basal melt in current-generation ECCO2 solutions also have implications for the global overturning circulation [*Hellmer*, 2004]. In this study, we evaluate versus independent, satellite-derived basal melt estimates the impact of (i) explicitly representing ice-shelf-ocean interaction and (ii) improving the vertical resolution of the ECCO2 model configuration. The goal is to gain an understanding of what aspects of ice-shelf-ocean interaction may be improved by an explicit representation of the processes at model resolutions that are typical of current-generation ocean reanalyses and IPCC simulations. We also discuss the remaining discrepancies and their causes.

The paper is organized as follows. First, we present the satellite observations of basal melt rate used for model evaluation. Second, we describe the ECCO2 model configuration and the two model sensitivity experiments. Third, we discuss the model simulation results and compare them to the observations. Fourth, we discuss the causes of model-data discrepancies in basal melt rate and patterns. We conclude with recommendations for future studies and for improved representation of ice-shelf-ocean interaction in ocean reanalyses and climate simulations.

2. RJMS Observations

Rignot et al. [2013, hereinafter RJMS] use the volume flux divergence of ice shelves in Antarctica, the surface mass balance (from regional atmospheric climate models), and the rate of ice shelf thickening (from laser altimetry) to determine melt rate and mass balance for the period 2003–2009 (Figure 1, top). They find that the basal melt of 1325 $\pm$ 235 Gt/a is larger than the total calving flux of 1089 $\pm$ 139 Gt/a and accounts for a larger fraction of Antarctic mass loss than previously thought. They also find that the large cold-water ice shelves in the Weddell and Ross Seas contribute only 15% of the net melt while about 50% of the basal melt originates from ice shelves in the Amundsen-Bellingshausen Seas (see Figure 2b for ice shelf locations). The latter region shows a high melt/area ratio, which is also found in several East Antarctic ice shelves. The

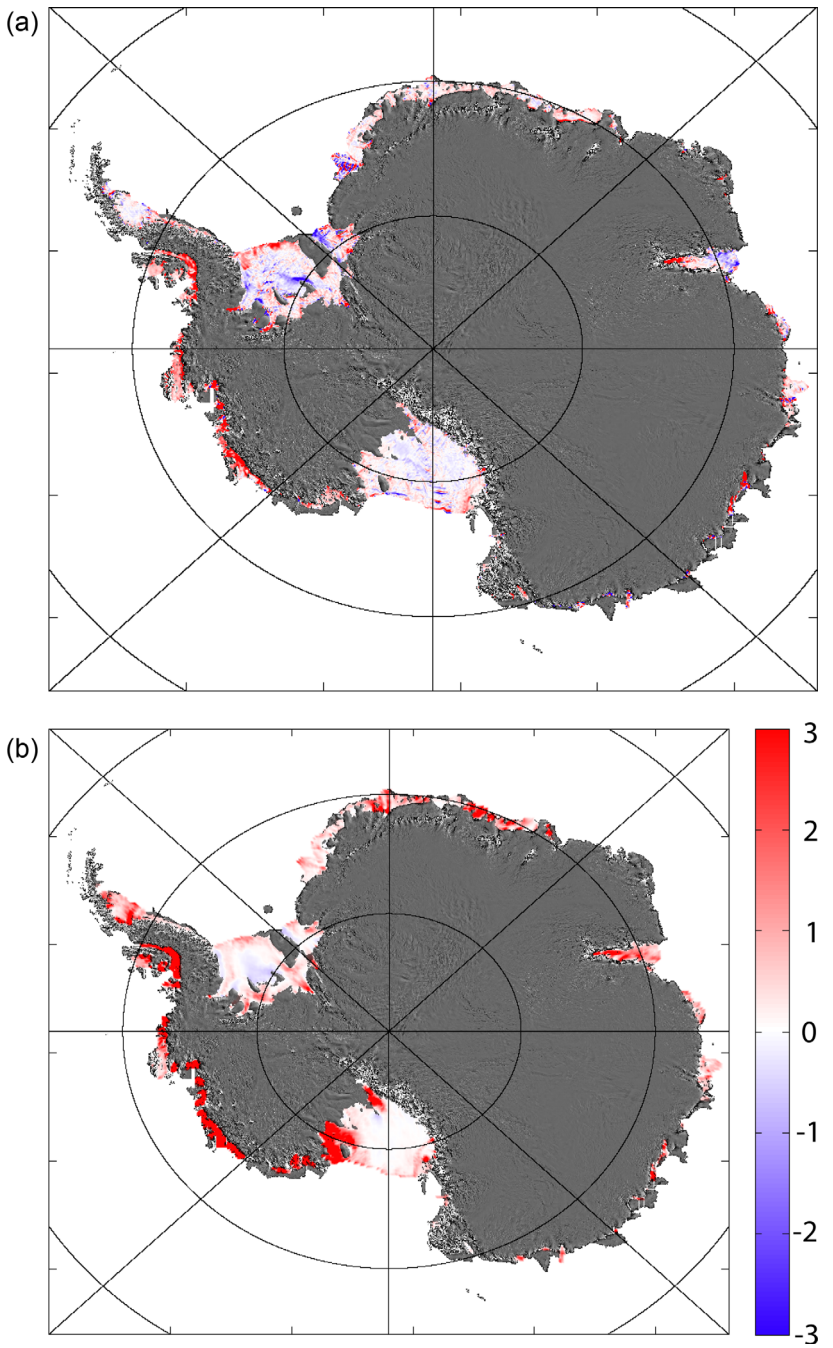

Figure 1. Mean circumpolar basal melt rates and pattern (m/a) for (top) RJMS and (bottom) simulation L100. Melt rates are color coded from < -3 m/a (freezing) to $> +3$ m/a (melting) and overlaid on an image of a MODIS mosaic of Antarctica (MOA) [*Haran et al.*, 2005].

highest melt rates are found in the Southeast Pacific Sector of the Antarctic Continent, ranging from George VI to Getz Ice Shelf (IS). On slow-moving to nearly stationary ice shelves like the Wilkins, George VI, Abbot, and Sulzberger IS, basal melting entirely consumes the inflow of individual glaciers within a few kilometers of their grounding zones. High melt rates are also revealed in the grounding zones of the Amery, Moscow University, Shackleton, and Totten IS in East Antarctica. Another finding is a complex spatial pattern of ice shelf melt water production around the continent, with an outsized contribution of smaller, fast-melting ice shelves in West and East Antarctica.

The RJMS freeze/melt distribution shows strongest basal melting near the grounding line/zone of the major ice shelves/glaciers and also along the ice fronts of some of the larger ice shelves. While the larger ice

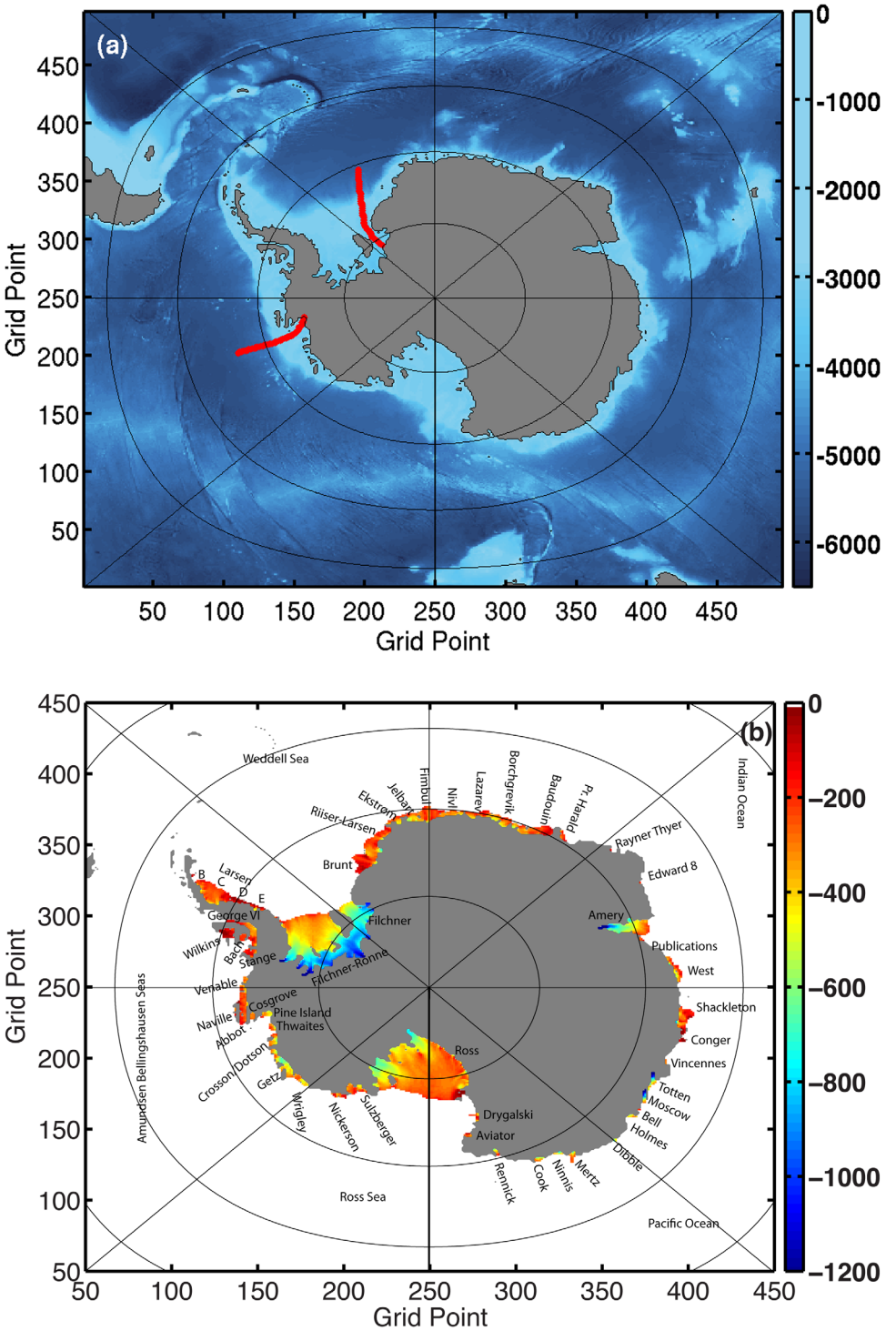

Figure 2. (a) Bathymetry (m) of circumpolar model domain. Red lines depict the section locations used in Figures 9 and 11. (b) Ice shelf thickness (m) for 50 ice shelves and glaciers.

shelves exhibit basal freezing and marine ice formation (negative melt rate), this only occurs in a few of the smaller, cold-water ice shelves. Freezing is often concentrated on the western sides, which is consistent with the physical processes of the ice pump, formation of ice shelf water, and its subsequent circulation in the sub-ice-shelf cavity. Meltwater production from several small East Antarctic ice shelves in the Wilkes Land sector is surprisingly large. Area-averaged melt rates from Dibble through Vincennes are comparable

to Amundsen Sea ice shelf melt rates from Crosson through Land, while meltwater produced by Shackleton and West IS rivals that from Thwaites and Sulzberger IS.

3. Circumpolar Model Configuration

The ECCO2 project produced a global-ocean and sea-ice data synthesis by constraining a global-ocean configuration of the Massachusetts Institute of Technology general circulation model (MITgcm) [*Marshall et al*., 1997] to a comprehensive compilation of the available ocean and sea ice data. The ocean/sea-ice model has horizontal grid spacing of approximately 18 km with 50 vertical levels in its original set up, whereby 20 levels are within the top 320 m. The model is volume conserving and uses a C-Grid finite volume discretization. The ocean component of the MITgcm is coupled to a sea ice model, as described in *Losch et al*. [2010]. In this study we used a circumpolar Southern Ocean domain from the global ECCO2 configuration in order to reduce computational cost while exploring the impact of ice-shelf-ocean interaction. Freezing/melting processes in the sub-ice-shelf cavity are represented by the three-equation thermodynamics of *Hellmer and Olbers* [1989] with modifications by *Jenkins et al*. [2001] and implemented in the *MITgcm by Losch* [2008]. Exchanges of heat and freshwater at the base of the ice shelf are parameterized as diffusive fluxes of temperature and salinity using a constant friction velocity and the turbulent exchange coefficients of *Holland and Jenkins* [1999].

In a first simulation (referred to as L050) the vertical and horizontal resolutions remain the same as in the global ECCO2 model configuration. In a second simulation (referred to as L100) we double the number of vertical levels to 100 in order to accommodate higher vertical resolution in the depth range of the ice shelf cavities and the continental shelf (200–1200 m).

The bathymetry (Figure 2, left) is a blend of *Smith and Sandwell* [1997] v14.1 and, south of 60°S, the International Bathymetric Chart of the Southern Ocean (IBCSO) [*Arndt et al*., 2013]. The latter includes the best possible data available in the ice shelf cavity (i.e., BEDMAP2) [*Fretwell et al*., 2013] and the most recent ship-based observations on the continental shelf.

With the chosen horizontal grid spacing, 50 ice shelves and glaciers are represented with at least 2 model grid points. Ice shelf thicknesses (Figure 2, right) are from *Griggs and Bamber* [2011] and grounding line locations from *Rignot et al*. [2011]. Interpolation onto the grid leads to under/overestimation of the ice shelf area compared to observed areas (see Table 1) due to the location of the grounding line with respect to the center of the grid cell. Ice front melting is not represented in this model set up as the ice front area is small compared to the area of the ice shelf base.

The MITgcm uses the partial cell formulation of *Adcroft et al*. [1997] to accurately represent the shape of the sea floor, the continental slope, and the base of ice shelves. Some adjustments to bathymetry and ice shelf thickness are necessary in areas with negative water column thickness (e.g., Totten Glacier) to allow exchange of water between the ice shelf cavity and the continental shelf. We apply a bottom boundary layer scheme that allows downslope flow of dense water masses into the abyss while limiting artificial numerical mixing due to the size of the vertical grid cells. Tidal forcing is not included.

In modeling ice-shelf-ocean interaction, we use the steady-state assumption where basal melting or freezing is balanced by glacier flow, and the ice shelf is treated as a rigid slab of ice with no flexural response or change of shape. Mass loss through calving of icebergs at the ice shelf front is assumed to be 2016 Gt/a [*Jacobs et al*., 1992], which is used in the ECCO2 project, and is different to the value estimated by *Rignot et al*. [2013]. This amount is added as surface freshwater flux near the Polar Front of the Antarctic Circumpolar Current (ACC), and the freshwater input due to iceberg melt is estimated to be small on the continental shelf [*Schodlok et al*., 2006; *Jansen et al*., 2007]. Hence, areas of interest are not likely to be affected by choosing the larger value. No estimates of glacial runoff exist for the ice shelf grounding lines nor the coastline in areas without ice shelves.

Initial and lateral boundary conditions are provided by the so-called "cube92" global-ocean and sea-ice ECCO2 simulation. Temperatures and salinities of the sub-ice-shelf cavities are prescribed where observations are available; otherwise the initial conditions are extrapolated from the cube92 initial conditions at the mouth of the cavities. The L050 and L100 simulations are started in 1992 and integrated to 2013, followed by a second set of integrations for the 1992–2013 period. As the cavity temperatures and salinities need

Table 1. Mean Basal Melt of Antarctic Ice Shelves for Period 1992 to 2013[a]

Ice Shelf	Area Mod	BMF 50	BML 50	BMF 100	BML 100	Lat	Lon	Area Obs	BMF Obs	BML Obs
Larsen-B	954	0.59 ± 0.71	0.5 ± 0.6	1.02 ± 0.95	0.9 ± 0.8	−65.55	298.58	6755	1.80 ± 2.0	12.2 ± 14
Larsen-C	64212	0.17 ± 0.04	10.4 ± 2.6	1.47 ± 0.24	87.0 ± 14.2	−67.46	297.27	46465	0.45 ± 1.0	20.7 ± 67
Larsen-D	9944	0.24 ± 0.52	2.2 ± 4.8	0.51 ± 0.46	4.7 ± 4.3	−70.24	298.42	22548	0.06 ± 0.6	1.4 ± 14
Larsen-E	7086	0.11 ± 0.41	0.7 ± 2.6	0.29 ± 0.47	1.9 ± 3.0	−73.40	298.92	1184	1.20 ± 0.9	1.4 ± 1
Ronne	323579	0.86 ± 0.14	258.1 ± 42.1	0.20 ± 0.02	59.7 ± 6.3	−78.45	296.49	338887	1.50 ± 0.6	191 ± 80
Filchner	128025	4.55 ± 0.34	534.6 ± 40.3	0.41 ± 0.04	48.6 ± 4.7	−80.28	317.71	104253	0.40 ± 0.1	41.9 ± 10
Brunt	39661	0.36 ± 0.11	13.1 ± 4.0	0.31 ± 0.11	11.3 ± 4.1	−74.93	337.39	36894	0.03 ± 0.2	1.0 ±6
Riiser-Larsen	45523	0.40 ± 0.09	16.7 ± 4.1	0.26 ± 0.09	10.8 ± 4.1	−73.13	343.52	43450	0.20 ± 0.2	8.7 ± 8
Ekstrom	11819	0.61 ± 0.15	6.7 ± 1.6	0.40 ± 0.16	4.4 ± 1.7	−71.04	351.38	6872	0.63 ± 0.2	4.3 ±2
Jelbart	14014	1.43 ± 0.30	18.4 ± 3.9	1.26 ± 0.41	16.2 ± 5.3	−70.88	355.34	10844	−0.09 ± 0.3	−1.0 ± 3
Fimbul	45255	1.33 ± 0.32	55.2 ± 13.5	1.13 ± 0.32	46.9 ± 13.6	−70.36	359.57	40843	0.57 ± 0.2	23.5 ± 9
Nivl	7801	0.46 ± 0.27	3.3 ± 1.9	0.11 ± 0.08	0.8 ± 0.6	−70.29	11.11	7285	0.54 ± 0.2	3.9 ± 2
Lazarev	15607	0.90 ± 0.26	12.9 ± 3.7	0.52 ± 0.32	7.4 ± 4.7	−69.93	14.47	8519	0.73 ± 0.2	6.3 ± 2
Borchgrevink	13695	2.74 ± 0.56	34.5 ± 7.1	2.92 ± 0.80	36.7 ± 10.1	−70.26	19.81	21580	0.35 ± 0.3	7.5 ± 6
Baudouin	38831	1.07 ± 0.42	38.1 ± 15.2	1.08 ± 0.55	38.5 ± 19.8	−70.06	28.89	32952	0.43 ± 0.4	14.1 ± 12
Weddell Sea	766013	1.43 ± 0.20	1005.6 ± 56.5	0.53 ± 0.33	375.9 ± 49.7	N/A	N/A	729331	0.89 ± 0.4	336.9 ± 108
Prince Harald	5597	2.56 ± 1.07	13.2 ± 5.5	2.54 ± 1.22	13.1 ± 6.3	−69.36	36.19	5392	−0.37 ± 0.6	−2.0 ± 3
Rayner Thyer	625	0.31 ± 0.20	0.2 ± 0.1	0.22 ± 0.18	0.1 ± 0.1	−67.73	48.45	641	10.46 ± 2.0	6.7 ± 1
Edward 8	627	−0.01 ± 0.01	−0.01 ± 0.01	−0.02 ± 0.001	−0.01 ± 0.00	−66.73	56.43	411	10.22 ± 2.0	4.2 ± 0.8
Amery	62850	1.13 ± 0.23	65.6 ± 13.5	1.25 ± 0.15	72.1 ± 9.1	−70.38	70.43	60654	0.58 ± 0.4	35.5 ± 23
Publications	1875	1.30 ± 0.46	2.2 ± 0.8	1.56 ± 0.50	2.7 ± 0.8	−69.76	75.16	1551	0.95 ± 1.0	1.5 ± 2
West	18497	1.57 ± 0.37	26.6 ± 6.3	0.87 ± 0.27	14.7 ± 4.7	−66.95	85.00	15666	1.74 ± 0.7	27.2 ± 10
Indian Ocean	90075	1.30 ± 0.32	107.9 ± 13.9	1.24 ± 0.39	102.7 ± 12.7	N/A	N/A	84315	0.86 ± 0.5	73.1 ± 25
Shackleton	34015	0.59 ± 0.33	18.4 ± 10.4	0.52 ± 0.32	16.2 ± 10.2	−65.98	97.50	26080	2.78 ± 0.6	72.6 ± 15
Conger	3205	0.69 ± 2.20	2.0 ± 6.5	0.80 ± 2.40	2.4 ± 7.1	−65.78	103.41	1547	2.31 ± 0.9	3.6 ± 1
Vincennes	1269	1.08 ± 0.47	1.2 ± 0.5	1.06 ± 0.48	1.3 ± 0.5	−66.72	109.95	935	5.34 ± 2.0	5.0 ± 2
Totten	8202	7.87 ± 1.11	59.2 ± 8.4	1.51 ± 0.55	11.4 ± 4.2	−67.06	115.70	6032	10.47 ± 0.7	63.2 ± 4
Moscow	5981	8.57 ± 2.02	47.0 ± 11.1	2.80 ± 1.01	15.4 ± 5.6	−67.01	120.27	5798	4.73 ± 0.8	27.4 ± 4
Bell	629	0.45 ± 0.67	0.2 ± 0.4	0.43 ± 0.64	0.2 ± 0.4	N/A	N/A	N/A	N/A	N/A
Holmes	2828	3.50 ± 0.84	9.0 ± 2.2	1.73 ± 0.39	1.9 ± 1.0	−66.78	127.22	1921	3.46 ± 2.0	6.7 ± 4
Dibble	1257	7.59 ± 1.56	8.7 ± 1.8	2.79 ± 0.78	2.0 ± 0.9	−66.24	134.74	1482	5.46 ± 0.9	8.1 ± 1
Mertz	6280	2.32 ± 0.47	13.4 ± 2.7	1.28 ± 0.29	7.4 ± 1.7	−67.26	145.35	5522	1.43 ± 0.6	7.9 ± 3
Ninnis	2503	4.53 ± 1.52	10.4 ± 3.5	1.25 ± 0.35	2.8 ± 0.8	−68.26	147.54	1899	1.17 ± 2.0	2.2 ± 3
Cook	4386	3.52 ± 0.93	14.1 ± 3.7	1.35 ± 0.39	5.4 ± 1.6	−68.56	152.74	3462	1.33 ± 1.0	4.6 ± 5
Pacific Ocean	70562	2.84 ± 1.01	183.9 ± 30.6	1.02 ± 0.69	66.4 ± 24.1	N/A	N/A	54624	3.68 ± 0.8	201.3 ± 18
Rennick	3421	0.57 ± 0.21	1.8 ± 0.6	0.08 ± 0.02	0.3 ± 0.06	−70.73	161.78	3273	2.15 ± 0.3	7.0 ± 1
Aviator/Mariner	3693	0.50 ± 0.19	1.6 ± 0.6	0.34 ± 0.19	1.1 ± 0.6	−73.91	165.44	3490	1.77 ± 0.3	1.4 ± 0.2
Drygalski/Nansen	4882	1.36 ± 0.46	6.1 ± 2.0	1.27 ± 0.47	5.7 ± 2.1	−75.39	163.37	4323	3.27 ± 0.5	7.6 ± 1
Ross	506413	0.41 ± 0.13	190.4 ± 63.8	0.36 ± 0.14	167.1 ± 68.3	−80.82	192.08	500809	0.25 ± 0.1	49.1 ± 14
Sulzberger	16357	5.69 ± 0.98	85.3 ± 14.8	5.33 ± 1.25	79.9 ± 18.7	−77.09	211.10	12333	1.48 ± 0.3	18.2 ± 3
Nickerson	6388	4.15 ± 1.21	24.3 ± 7.2	3.77 ± 1.07	22.1 ± 6.3	−75.80	214.19	6495	0.64 ± 0.3	4.2 ± 2
Wrigley	9155	12.12 ± 1.88	101.7 ± 15.8	9.53 ± 1.54	79.9 ± 12.9	N/A	N/A	N/A	N/A	N/A
Ross Sea	550312	0.81 ± 0.32	411.2 ± 30.5	0.51 ± 0.17	356.1 ± 30.0	N/A	N/A	530722	0.33 ± 0.1	87.5 ± 14
Getz	26903	12.33 ± 1.01	303.9 ± 25.0	11.05 ± 0.81	272.4 ± 20.1	−72.35	290.38	34018	3.80 ± 0.7	89.0 ± 17
Crosson/Dotson	9778	8.10 ± 0.76	72.6 ± 6.8	5.85 ± 0.68	52.4 ± 6.2	−75.00	249.63	9032	11.92 ± 1.0	38.5 ± 3
Thwaites	4885	13.87 ± 2.74	62.1 ± 12.3	8.84 ± 1.94	39.6 ± 8.7	−75.07	253.59	5499	17.73 ± 1.0	97.5 ± 7
Pine Island	6725	19.38 ± 1.98	119.4 ± 12.2	14.91 ± 1.04	91.9 ± 6.5	−74.93	259.28	6249	16.20 ± 1.0	101.2 ± 8
Cosgrove	3997	11.98 ± 2.13	43.8 ± 7.8	8.80 ± 1.45	32.2 ± 5.3	−73.53	259.54	3033	2.79 ± 0.7	8.5 ± 2
Abbot	33030	2.05 ± 0.57	62.0 ± 17.4	1.23 ± 0.44	37.2 ± 13.4	−72.79	263.63	29688	1.75 ± 0.6	51.8 ± 20
Naville	1549	1.10 ± 0.31	1.5 ± 0.4	0.61 ± 0.27	0.9 ± 0.4	N/A	N/A	N/A	N/A	N/A
Venable	3699	12.87 ± 2.01	43.6 ± 6.8	8.52 ± 2.60	28.9 ± 8.8	−73.09	272.81	3194	6.07 ± 0.7	19.4 ± 2
Stange	9234	3.92 ± 0.46	33.1 ± 3.9	3.03 ± 0.38	25.6 ± 3.2	−73.22	283.33	8027	3.49 ± 0.7	28.0 ± 6
Bach	5255	4.13 ± 0.80	19.9 ± 3.8	6.15 ± 0.74	29.6 ± 3.6	−72.04	287.90	4579	2.28 ± 0.3	10.4 ± 1
Wilkins	15574	1.71 ± 0.83	24.4 ± 11.9	1.53 ± 0.70	21.8 ± 9.9	−70.49	287.93	12866	1.46 ± 1.0	18.8 ± 16
George VI	27469	14.82 ± 0.68	373.1 ± 17.1	7.99 ± 0.88	201.2 ± 22.3	−74.41	235.62	23434	4.26 ± 0.4	144.9 ± 13
Am Bel Sea	148103	8.54 ± 1.19	1159.9 ± 51.5	6.14 ± 0.99	833.82 ± 47.5	N/A	N/A	139619	4.82 ± 0.7	599 ± 35
Total Antarctica	1625065	0.61 ± 0.15	2868.6 ± 183.1	0.37 ± 0.09	1735.0 ± 164.1	N/A	N/A	1553978	0.85 ± 0.1	1325 ± 235

[a]Latitude (Lat), longitude (Lon), and area (km^2) are taken from RJMS. Average means of Basal Ice Mass Flux (BMF, m/a), and total Basal Mass Loss (BML, Gt/a) using an ice density of 917 kg m^{-3}; BMF, and BML with suffix 50 refer to Model Run L050, with suffix 100 to Model run L100, and suffix Obs to observations. Positive values indicate melting (mass loss), and negative values indicate refreezing (mass gain).

adjustment from initial conditions, the first 22 years are taken as spin-up and only the second cycle is used for analysis. Under the large ice shelves temperatures and salinities of the cavities reached quasi-steady-state within the first few years of integration. The boundary conditions for sea ice and ocean include temperature, salinity, and horizontal velocity fields. Surface forcing fields are from the Japanese 25 year

Reanalysis and the Japan Meteorological Agency Climate Data Assimilation System (JRA-25 and JCDAS) [*Onogi et al*., 2007].

The 18 km horizontal grid spacing of the model cannot resolve eddy activity on the Antarctic continental shelf and near the ice shelves; hence eddies are parameterized using the *Redi* [1982] and *Gent and McWilliams* [1990] schemes. We use the flux-limited, seventh-order, monotonicity-preserving advection scheme of *Daru and Tenaud* [2004] and horizontal viscosity follows the modified Leith scheme of *Fox-Kemper and Menemenlis* [2008]. Bottom-drag is quadratic, side-drag is free-slip, and vertical viscosity and diffusivity are parameterized according to the K-profile parameterization (KPP) of *Large et al*. [1994].

4. Circumpolar Model Results

In this section, we present the main circumpolar model characteristics, that is, the large-scale ocean circulation, water mass properties, and sea ice distribution and thickness.

4.1. Ocean Circulation

The main features of the large-scale Southern Ocean circulation include the ACC, and the Weddell, Ross, and Kerguelen Gyres. Drake Passage transport is used to indicate the strength of the ACC. Estimates of Drake Passage transport range from 133.8 ± 11.2 Sv [*Whitworth*, 1983; *Whitworth and Peterson*, 1985] to 154 ± 38 Sv [*Firing et al*., 2011]. The simulated mean Drake Passage transports are 136 ± 7 Sv for L050 and 149 ± 6.4 Sv for L100. The L050 transport shows a drift of 0.4 Sv/yr. This drift is caused by a freshening of Antarctic continental shelf waters in L050 due to an overestimation of melt rates. The enhanced freshwater input raises sea level near Antarctica, reduces the meridional sea level gradient, and hence reduces Drake Passage transport.

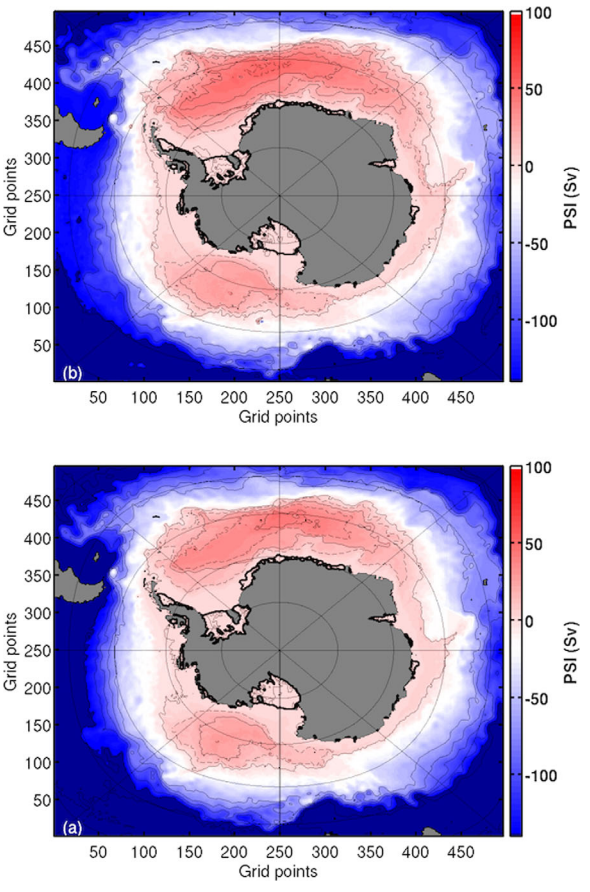

Figure 3. Time-mean horizontal stream function for (a) L050 and (b) L100.

The simulated Southern Ocean Gyres (Weddell, Ross, and Kerguelen, Figure 3) are less symmetric, more elongated, and shifted to more southerly locations compared to previous modeling studies [e.g., *Beckmann et al*., 1999; *Timmermann et al*., 2002]. The double cell structure of the Weddell Gyre, as shown by observations and model studies [*Mosby*, 1934; *Beckmann et al*., 1999], is reproduced in the simulations as a seasonal and interannual feature and less disctinct in the mean shown in Figure 3. The western cell is smaller in size and transport compared to the larger more elongated eastern cell, and is more pronounced in L050. For L100 both cells are lower in magnitude (east: 50.5 ± 9 Sv, west: 42.5 ± 8 Sv) compared to L050 (east: 58.8 ± 9 Sv, west: 46.4 ± 8 Sv). Furthermore, L050 has an additional gyre maximum (53.6 ± 8 Sv) centered around 25°W appearing intermittently in between the main cells. This gyre is less well defined in L100 (42 ± 8 Sv). On the continental shelf a cyclonic gyre is established over the Filchner Trough with higher transports for L050 (3.66 ± 0.60 Sv) compared to L100 (1.62 ± 0.32 Sv).

The simulated Weddell Gyre transport can be compared to observation-based estimates. *Schröder and Fahrbach* [1999] estimated 60 ± 10 Sv for the eastern cell along the

Greenwich Meridian. *Klatt et al.* [2005] found 45 ± 7 Sv and 56 ± 8 Sv for, respectively, the northern and southern limbs of the Weddell Gyre. *Fahrbach et al.* [1994] estimated a transport of 30 ± 10 Sv for the western cell along the Kapp Norvegia-Joinville Island section. This section does not cross the maximum of the gyre and thus the lower value.

The Ross Gyre transport (L100: 33.5 ± 8 Sv, L050: 37.8 ± 8 Sv) is larger than in previous model estimates (e.g., ∼20 Sv) [*Assmann and Timmermann*, 2005] while the Kerguelen Gyre (L100: 12.5 ± 9 Sv, L050: 17 ± 11.5 Sv) is less well defined as a gyre and also low in transport (compare with, e.g., ∼45 Sv, *Beckmann and Timmermann* [2001]).

4.2. Water Masses

In this section, we evaluate the simulated Temperature and Salinity (T/S) characteristics and the volume of major water masses in the Weddell Sea. The water mass structure of the circumpolar model domain reflected in the T/S diagram (Figure 4) reveals the main differences between the two runs and the World Ocean Atlas 2009 (WOA09) [*Locarnini et al.*, 2010; *Antonov et al.*, 2010]. The T/S diagram shows the improvements of doubling the number of vertical levels in the water mass structure on the continental shelf. While surface water masses (Antarctic Surface Water, AASW) and warm intermediate water masses (Circumpolar Deep Water, CDW) are well represented, High Salinity Shelf Water (HSSW, see water mass definitions in Table A1, Appendix A) is underrepresented in both model simulations. Although the sea ice model produces dense water masses through brine rejection on the continental shelf, the generated water mass remains in the Low Salinity Shelf Water (LSSW) class for L050. For L100, the salinity of sea-ice affected waters increases toward salinities in the lower salinity class of HSSW (Figure 4). The volume of LSSW in the Weddell Sea is larger for L050 compared to L100 (Figure 5); HSSW is almost absent in L050. In L100, HSSW is mainly present in the lower salinity class compared to observations. The lack of higher salinities in HSSW has consequences for bottom water production, which is missing in L050. In fact, Weddell Sea Bottom Water (WSBW) is gradually eroded during the integration [see also *Dotto et al.*, 2014]. WSBW is not replenished by sea ice formation and mixing with WDW (Warm Deep Water); instead it forms a less dense water mass that descends to mid depths to form WSDW (Weddell Sea Deep Water) class waters. In the case of L100 the volume of WSBW is renewed and hence its volume maintained (Figure 5). Figure 5a also shows the interannual variability of HSSW and WSBW and hence their close relationship. The HSSW curve has a maximum in 2001 and two minima in 1996 and 2009, while WSBW has a maximum in 2002 and two minima in 1997 and 2011. The interannual variability of LSSW shows a less distinct cycle (Figure 5b). It exhibits a minimum at the beginning of the time series

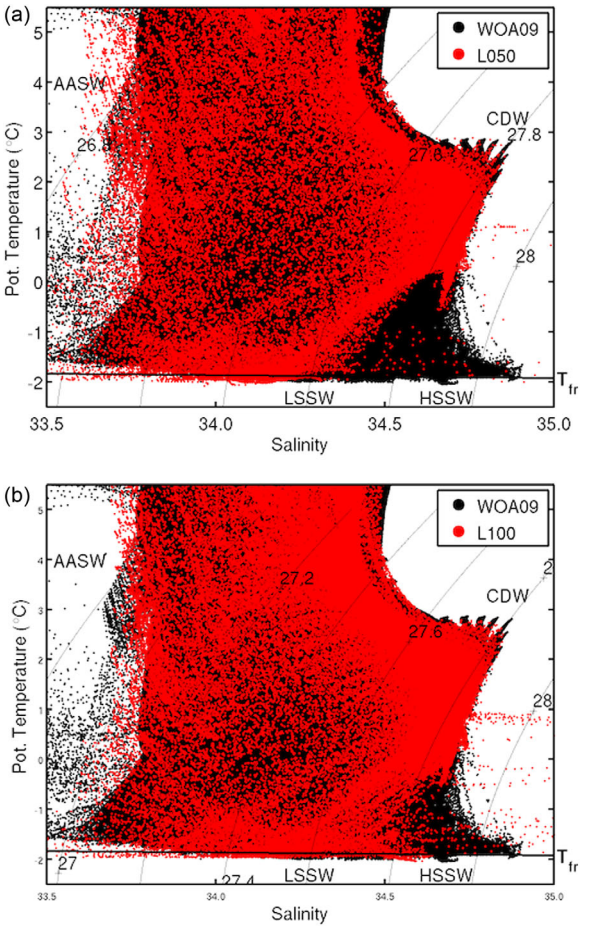

Figure 4. T/S diagrams of Southern Ocean Domain, excluding ice shelf cavities, for annual mean World Ocean Atlas (black, data interpolated onto model grid) and time-mean model output (red) of (a) L050 and (b) L100. The dots represent T and S at each grid cell. The main water masses (AASW-Antarctic Surface Water, CDW-Circumpolar Deep Water, HSSW-High Salinity Shelf Water, and LSSW-Low Salinity Shelf Water) are indicated on the figures. The black line marked T_{fr} at bottom of each diagram indicates the surface freezing point temperature.

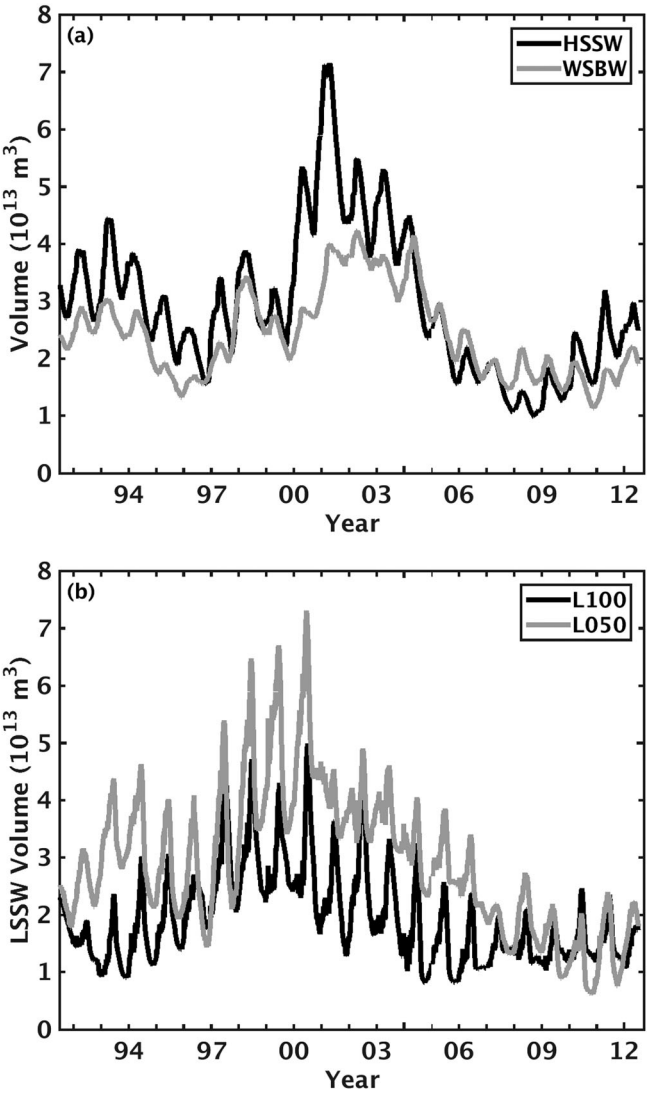

Figure 5. Weddell Sea water mass volume of (a) High Salinity Shelf Water (HSSW, black) and Weddell Sea Bottom Water (WSBW, gray) for the period 1992–2013 for simulation L100 and (b) Low Salinity Shelf Water (LSSW) for simulations L050 (gray) and L100 (black).

and a maximum in 2001. The later part of the time series shows no distinct minimum but rather a period of low LSSW formation. The seasonal cycles of HSSW and LSSW show a lag of about 2 months for LSSW with respect to HSSW. It remains to be seen whether this is a transformation of HSSW into LSSW or independent formation processes.

4.3. Sea Ice Properties

Sea ice area and extent (defined where the sea ice concentration is larger than 15%) are well represented in both the L050 and L100 simulations for seasonal (Figure 6, right) as well as interannual variability (not shown here). The mean sea ice area in L100 of 10.2×10^6 km^2 (sea ice extent: 12.13×10^6 km^2) is 2.1% (2.9%) larger than SSM/I-derived values. While the interannual variability of sea ice area and extent matches observations, the seasonal cycle is slightly offset (Figure 6). The September sea ice maximum occurs 5 days later and February sea ice minimum 13 days later than observed. The disintegration of the sea ice occurs quicker compared to SSM/I data but the growth phase of sea ice is comparable. There are longer periods of stagnation in the maximum/minimum phase. The steeper freezing and melting of sea ice is caused, in part, by the zero-layer thermodynamic sea ice model, which does not account for sensible heat storage in the ice [cf. *Losch et al.*, 2010, Figure 7]. The September sea ice area minimum is lower by 20% and the maximum February sea ice area is larger by 14%. The circumpolar sea ice edge with concentrations less than 50% is only slightly overestimated in September (2%); in February the extent is lower by 14%. The largest differences in simulated summer sea ice area compared to SSM/I data are found in the Pacific Ocean sector (∼35% overestimation) and the Amundsen-Bellingshausen Sea sectors (∼46% overestimation). For September sea ice areas, the largest differences occur in Indian and Pacific Ocean sectors with, respectively, ∼12% and ∼15% overestimation. The smallest differences in February and September sea ice area are found in the Weddell Sea sector with lower values in L100 compared to L050. Sea ice production between simulations differs by about 8% (L050 > L100). Sea ice thickness is larger by up to 22 cm in the north-western Weddell Sea (Weddell Scotia Confluence) for L050 and by up to 57 cm in the southern Weddell Sea for L100 (not shown here). This shift in ice volume between L050 and L100 primarily results from the stronger Weddell Gyre circulation of L050.

5. Ice Shelf-Ocean Interactions

The mean L100 circumpolar melt rate of 1735 ± 164 Gt/a is consistent within error bars with the 1325 ± 235 Gt/a derived from satellite observations by RJMS (Figure 7 and Table 1). In the L050 simulation,

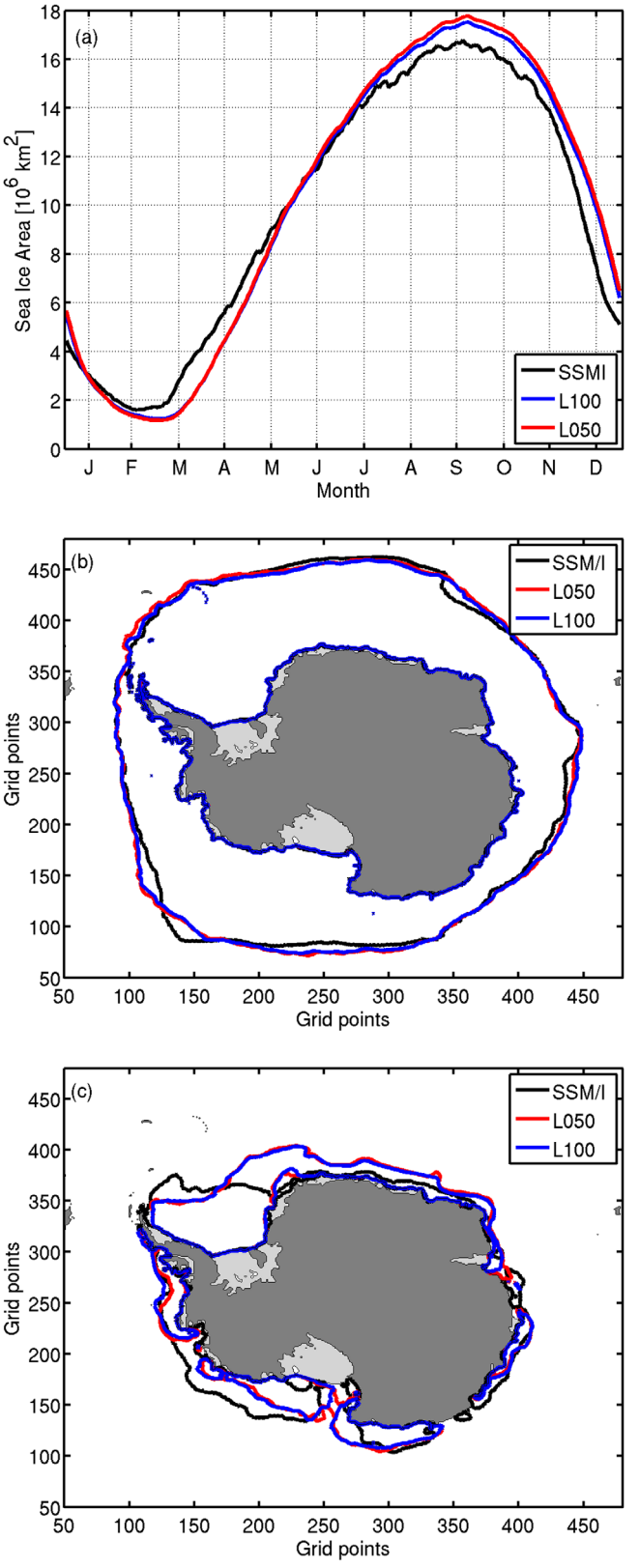

Figure 6. (a) Mean seasonal cycle of sea ice area, (b) mean September sea ice extent, and (c) mean February sea ice extent for simulations L050 and L100 compared to SSM/I-derived estimates. Note that the sea ice area differences between runs are small compared to the difference with observed sea ice area.

however, the amount of freshwater input through ocean-ice shelf interaction into the Southern Ocean is too high: 2868 ± 183 Gt/a. While the overall freshwater input in L100 is close to observed values, the melt pattern is only well represented in certain regions. On the one hand, cold water ice shelves in this model configuration have a large areal extent, i.e., they are represented by a large number of grid points. Also, the large ice shelves have been extensively surveyed during the last decades, which leads to a better knowledge of cavity bathymetry, ice shelf thickness, cavity hydrography, etc. For these reasons, the L100 estimates of melt rates and pattern are closer to the observed ones. On the other hand, warm water ice shelves are less well represented with respect to grid points and associated grid spacing and hence, in addition to misrepresentations of turbulent exchanges [*Dansereau et al.*, 2013], the discrepancy to observations in terms of melt rate and pattern is expected to be larger.

The temporal variability of basal melt on daily to interannual time scales is largest near the ice shelf front. Although melt rates at the grounding line are highest, their temporal variability is small. Even with better-resolved ice shelves, the large variability at the ice shelf edge is not easily transferred to the grounding line [e.g., *Schodlok et al.*, 2012]. *Khazendar et al.* [2013] showed that coastal polynya and sea ice formation associated with them, alter the dense shelf waters that can enter the sub-ice-shelf cavities. This changes the heat content available for basal melt. In the L050 and L100 simulations, coastal polynya formation is restricted to a small number of places, e.g., off the Ronne IS. In other areas with observed polynya formation, the horizontal resolution is too coarse to allow a coastline representation that favors polynya formation, e.g., off Sabrina Coast near

Totten Glacier. Also, the coarse horizontal grid spacing (~125 km) of the surface forcing does not resolve katabatic winds, which limits the capability to model polynya formation.

In the following section, we present more detailed basal melt rates in the Southern Ocean sectors defined by *Zwally et al*. [2002] with the exception that the eastern bound of the Weddell Sea Sector is slightly modified to include all ice shelves located along the coast of Queen Maud Land, i.e., it is 45°, here as opposed to 20°, in *Zwally et al*. [2002].

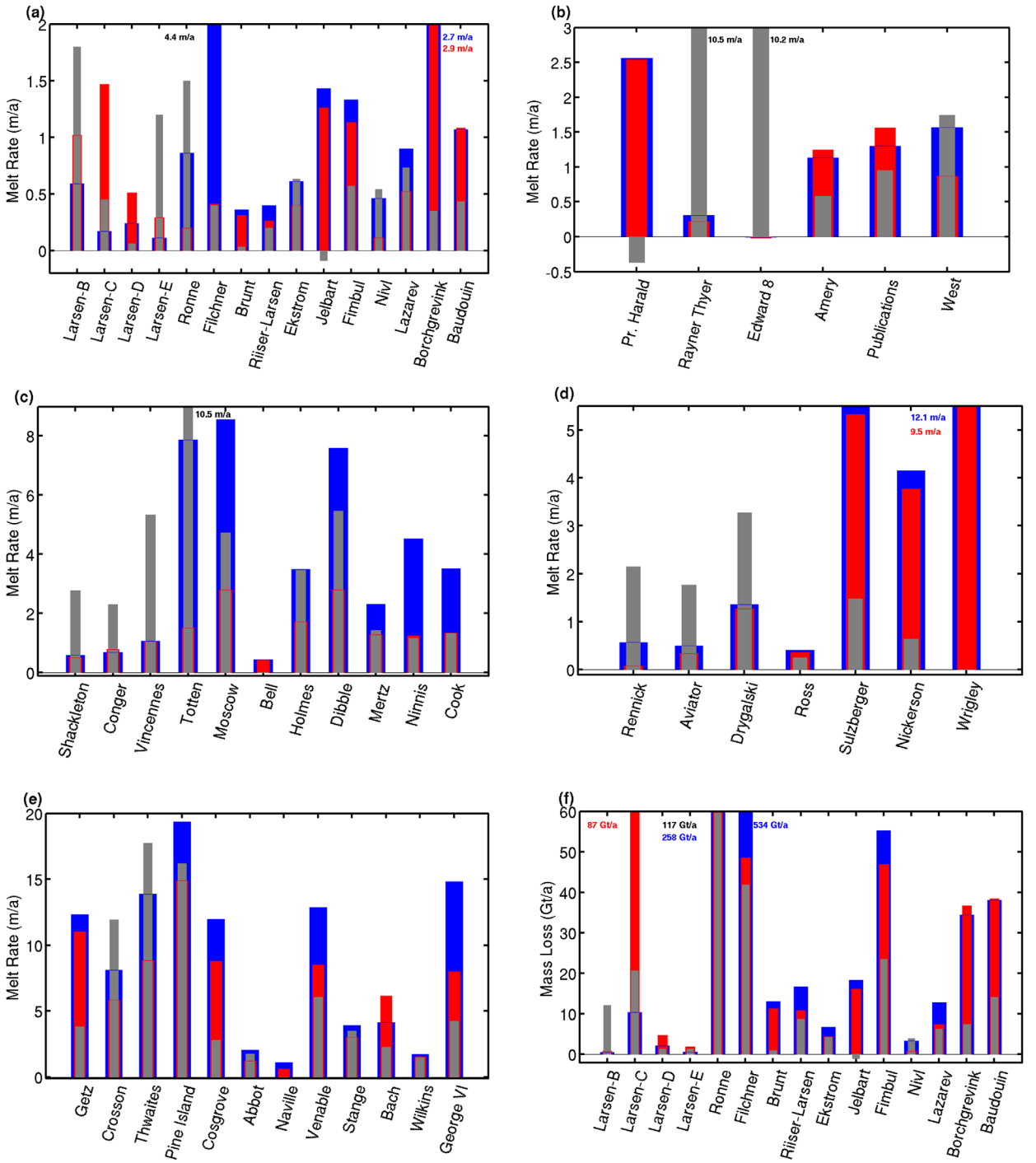

Figure 7. Mean basal melt rate (m/a; left column) and mean basal mass loss (Gt/a; right column) for the five sectors of the Southern Ocean (from top to bottom: Weddell Sea, Indian Ocean, Pacific Ocean, Ross Sea, and Amundsen-Bellingshausen Seas). Estimates are from RJMS (gray), L050 (blue), and L100 (red). Note that y axis ranges are different for each sector.

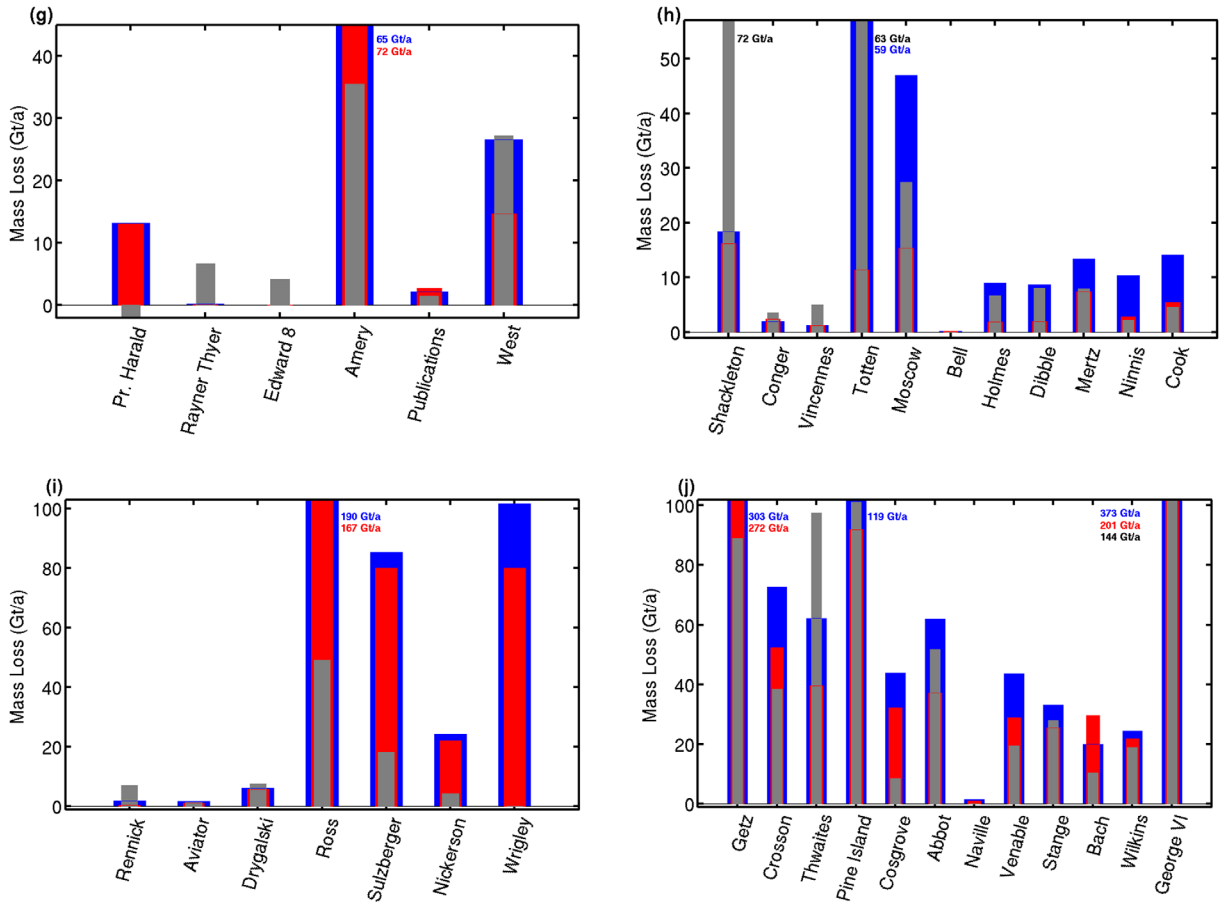

Figure 7. (continued)

5.1. Weddell Sea

The Weddell Sea sector comprises two distinct regions, the Southwestern and the Eastern Weddell Sea. The Eastern Weddell Sea Ice Shelves (EWIS) include those ice shelves that have a narrow continental shelf just to the north. They are in close vicinity to WDW, which is a potential source of heat that may enter the cavities (as shown by, e.g., *Nicholls et al*. [2006]) and contributes to basal melting. In the southwestern Weddell Sea a wide continental shelf with cold water masses may shield the sub-ice-shelf cavities from WDW.

The major ice shelf in this sector is the Filchner Ronne IS. Its melting and freezing pattern is similar (L100) not only compared to the recent RJMS pattern, but also to the one estimated by *Joughin and Padman* [2003]. The Ronne IS shows basal melting close to the grounding line in the deep channels, as described in RJMS, and considerable refreezing of marine ice near the Henry and Korff Ice Rises. The area-averaged melt rates are larger than observations in L050 (0.86 ± 0.14 m/a) because of an area of very high melt to the west of Berkner Island. In L100, the areas of melt and freeze are similar in size leaving a lower average (0.20 ± 0.02 m/a), which is below observed values (0.30 ± 0.1 m/a). However, the melt and freeze patterns match better in L100, with the spatial minima and maxima being smaller in magnitude by about 2 m/a (Figure 8, left column).

Compared to observations the Filchner IS melting is better represented in simulation L100 (Figure 7 and Table 1). A mass loss of 534 ± 40 Gt/a in L050 means an overestimation by a factor of 10. In contrast, a mass loss of 48.6 ± 4.7 Gt/a in L100 is closer to the RJMS estimate of 41.9 ± 10 Gt/a. This, in turn, has consequences for the Larsen IS, which is located downstream. The larger amount of fresh and cold water in L050 may contribute to a smaller influence of WDW on continental shelf waters, i.e., there is less heat available that

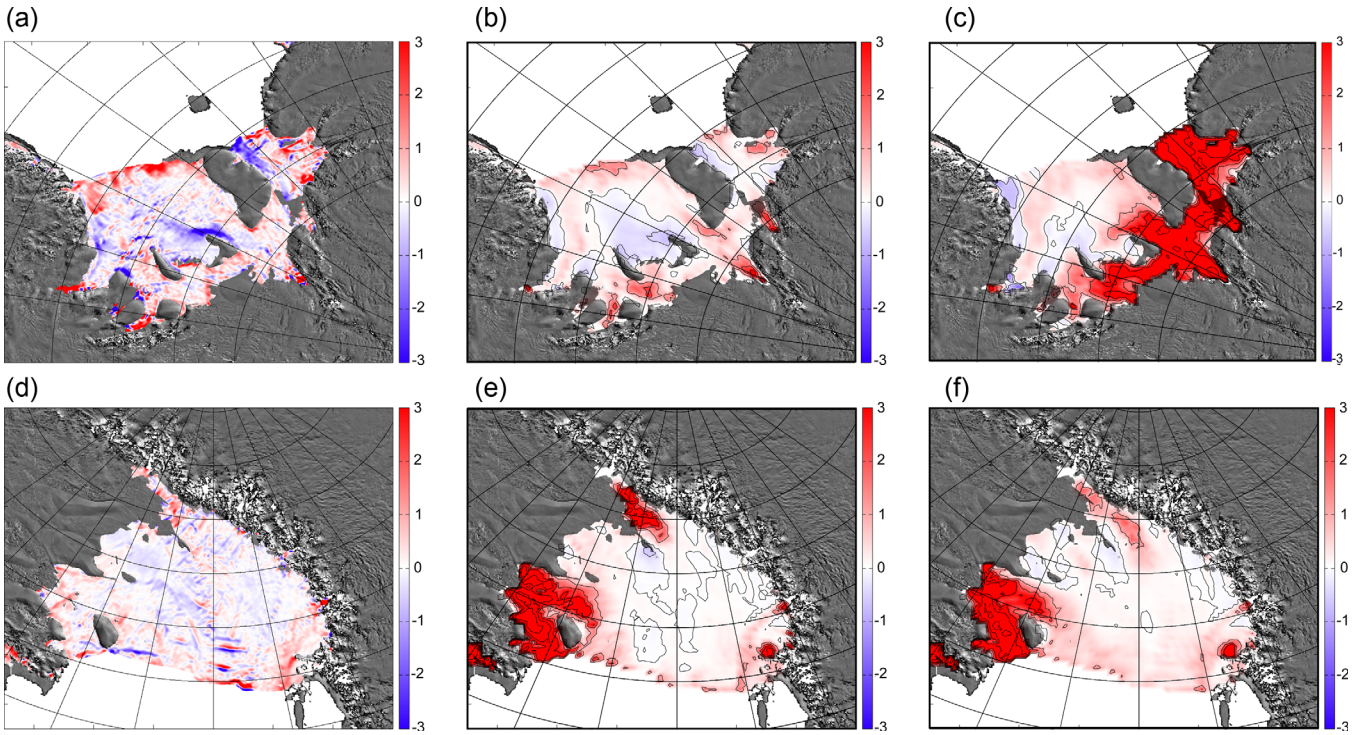

Figure 8. Mean basal melt rates (m/a) for Filchner Ronne (left column) and Ross (right column) ice shelves for (top) RJMS, (middle) L100, and (bottom) L050. Negative melt rates indicate freezing and positive indicate melting. Land imagery is from MODIS mosaic of Antarctica (MOA) [*Haran et al.*, 2005]. Contour intervals for model output are 1 m/a for positive and 0.5 m/a for negative values.

can add to Larsen IS melting. The melt rate for Larsen-C as the largest portion of the ice shelf is 0.17 ± 0.04 m/a in L050. By reducing this amount of fresh and cold water in L100, the melt rate of Larsen-C IS increases to 1.47 ± 0.24 m/a. This is contrary to most ice shelf melt rates, which decrease with increasing vertical levels. Larsen-C IS mass loss increases from 10.4 ± 2.6 Gt/a in L050 to 87.0 ± 14.2 Gt/a in L100 compared to 20.7 ± 67 Gt/a in RJMS. The melt pattern of Larsen-C IS, however, shows little resemblance to RJMS, who reveal a large area of marine ice formation in the southern part of the ice shelf. The model includes refreezing in the northern part and a small area in the southern part close to the Larsen-D IS. This is due to inflowing water masses that originate from the southern Weddell Sea continental shelf.

Temperature and salinity characteristics of the water masses in the Filchner-Ronne cavity are different between the two runs (Figures 9 and 10a). In L050, the Filchner and Ronne parts of the cavity are well separated, with higher temperatures and salinities in the Filchner part and lower temperatures and salinities in the Ronne part. Exchanges between the Filchner and Ronne cavities are seen in the T/S mixture between the two cavities. In L100, the T/S characteristics are more compact and the two subcavities cannot be distinguished in the T/S diagram (Figure 10a). Furthermore, the L100 T/S values are well below the surface freezing point temperature at higher salinities. With increased melting in the Filchner Ronne Cavity in L050, the T/S curve is stretched to lower salinities. At the higher salinity part of the L050 T/S characteristics, the warmer WDW is able to enter the cavity leading to temperatures of around -1°C. The water column in the L050 cavity is more heterogenous and more stratified stretching the T/S characteristics over a larger density range. In L100, the water column is more homogeneous below the surface freezing point temperature (T_f) in most parts of the cavity, except at the ice shelf front where warmer surface water masses ($T > T_f$) lead to melting (Figure 10).

A section along the Filchner Trough from the deep Weddell Sea into the Filchner cavity (Figure 9) illustrates the differences of water mass characteristics on the continental shelf and in the cavity. T/S Measurements south of Berkner Island [*Nicholls et al.*, 2001] indicate cold temperatures below the surface freezing point with little seasonal variability [*Nicholls*, 2004] over the entire water column. Considering the deep cavity part

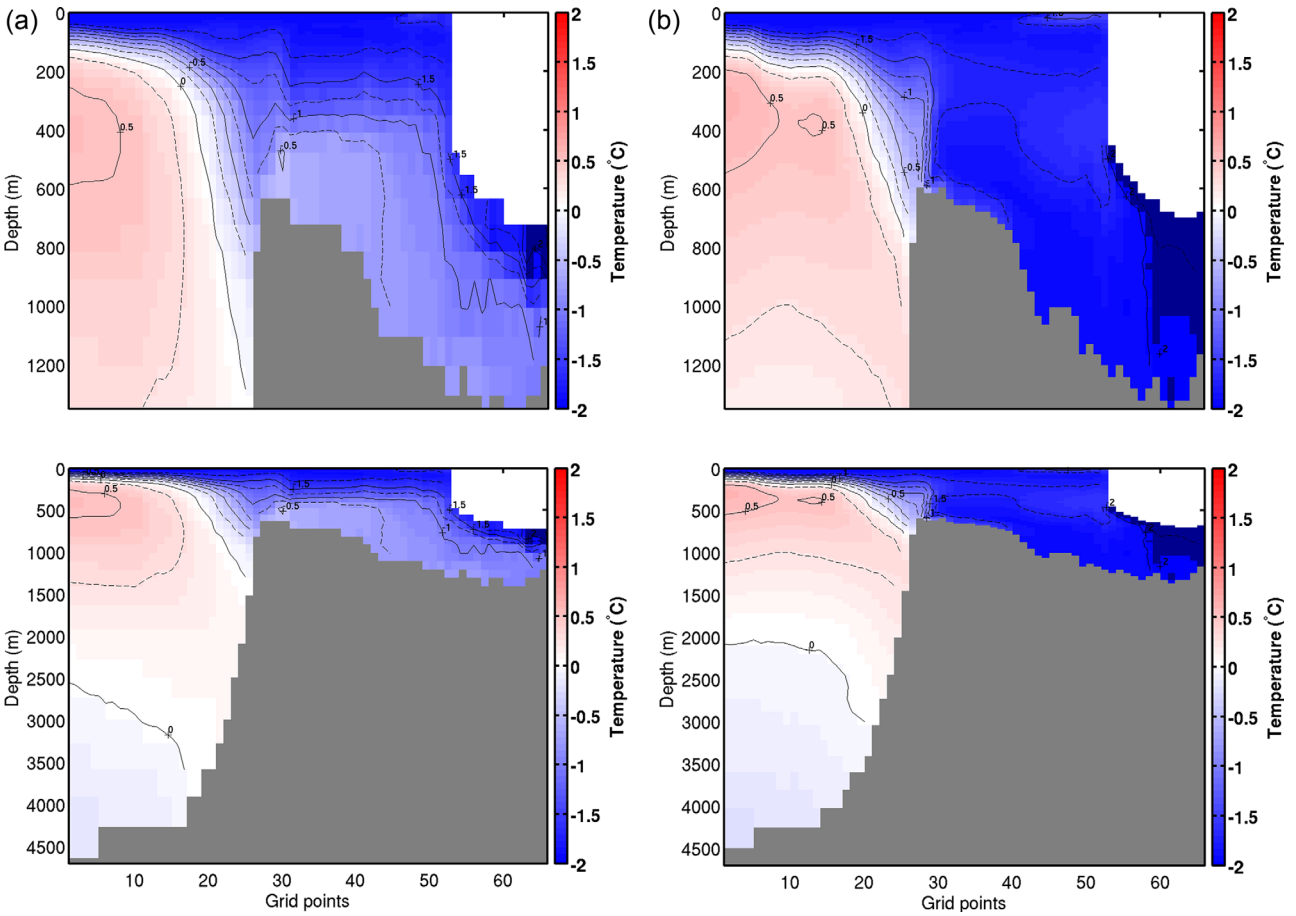

Figure 9. Section of mean temperature (°C) along Filchner Ice Shelf covering the deep Weddell Sea onto the continental shelf and into the sub-ice-shelf cavity for simulation (a) L050 and (b) L100. Land is shaded gray and ice shelf in white. Section location is indicated in Figure 2. (top) Top 1300 m and (bottom) the entire water column depth.

of the section (Figure 9, grid point 64) to be in the vicinity of the measurement location, L050 temperatures are warmer than the surface freezing point, with a warm inflow at the bottom of the cavity. In contrast L100 temperatures are well below the surface freezing point being homogenous throughout the water column. Overall, L050 temperatures at the base of Filchner IS are about 0.5°C warmer than in L100.

The water column on the continental shelf shows the stratified ocean with a distinct pycnocline in L050, while L100 shows the more mixed, homogenous water column. Both simulations show a strong frontal component at the continental shelf break. The structure of L100 resembles the frontal structure shown in *Nicholls et al*. [2003] more closely. It is likely that due to the misrepresentation of the frontal structure in L050, more warm water can penetrate onto the continental shelf and into the cavity, hence an increase in basal melt.

EWIS consists of a series of small ice shelves. It is unclear whether the sub-ice-shelf cavities are linked or separated from each other by bathymetric features. As only a few of these ice shelves are well studied (e.g., Fimbulisen) [*Hattermann et al*., 2012] the geometry of most cavities is not well known. The mean modeled melt rate of this part is 1.13 ± 0.32 m/a for L100 and 1.33 ± 0.32 m/a for L050 compared to 0.46 m/a for RJMS. The Temperature and Salinity variability along the coastal current on the continental shelf in front of the Weddell Sea ice shelves is not large and thus the mean melt rates along these ice shelves rather is uniform. The T/S characteristics of L050 and L100 in the cavities of the eastern Weddell Sea are not distictly different (Figure 10), hence the reduction of basal melt rate by 0.3 m/a from L050 to L100 is due to the thinner levels in the L100 cavity. Thinner levels mean that less heat is available to contribute to melting at the base of the ice shelves.

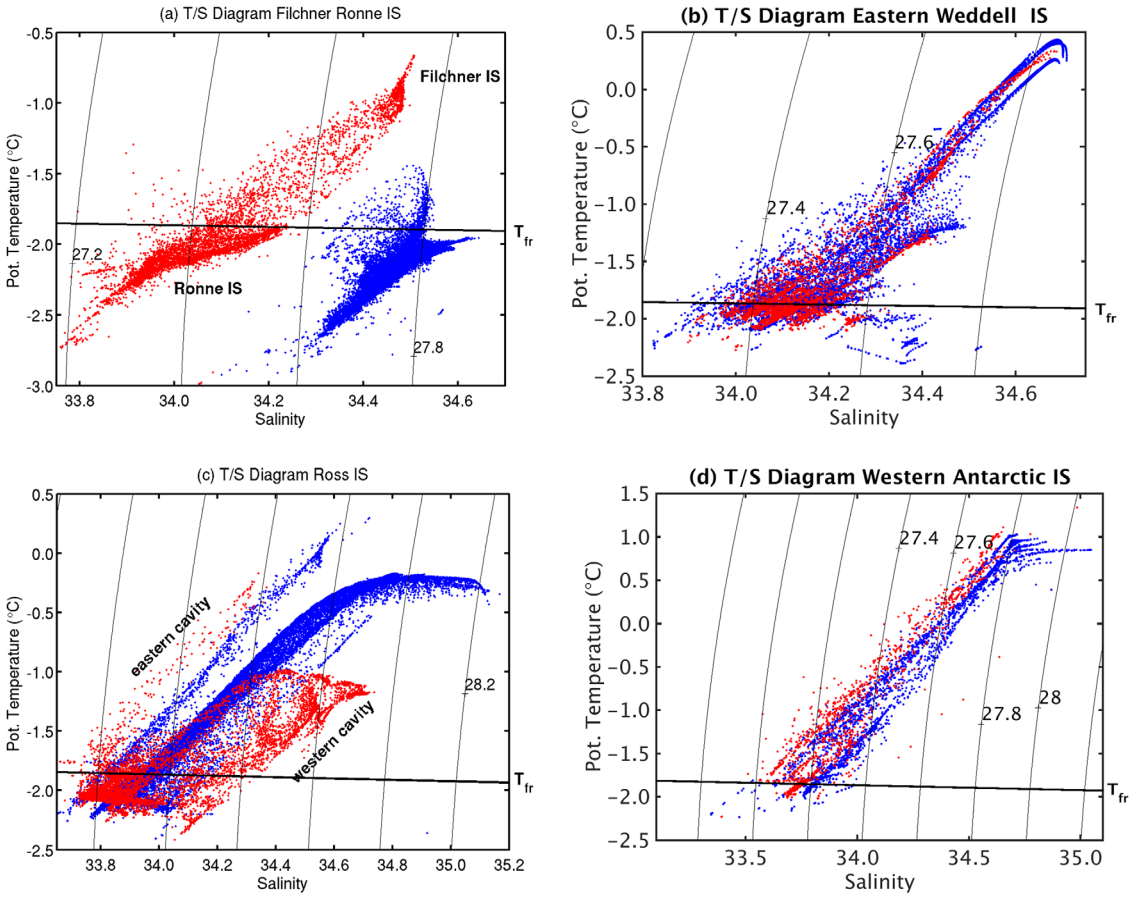

Figure 10. Time-mean T/S Diagrams for selected ice shelf cavity regions (a) Filchner Ronne, (b) Eastern Weddell (EWIS), (c) Ross, and (d) Amundsen-Bellingshausen Seas (WAIS). Red depicts T/S space for L050 and blue for L100. The dots represent T and S at each grid cell.

All 12 ice shelves located in the eastern Weddell Sea show a positive trend (both runs) in basal melt rates for the period 1992–2013. This trend is in agreement with a warming trend of the WDW [*Smedsrud*, 2005] and is a likely reason for the increase in basal melting of Fimbulisen.

5.2. Indian Ocean Sector

The melt rate in the Indian Ocean Sector ranges from 0.22 m/a to 2.54 m/a and has the smallest deviation from observed mean melt rates (1.24 m/a in L100 versus 1.09 m/a in RJMS). The smaller ice shelves, Rayner and Edward 8, have negligible melt rates, which is due to the size of the ice shelves on the model grid. In the observations, these two ice shelves have the highest melt rates (∼10 m/a) in this sector but the freshwater contribution (∼5 Gt/a) may have local influences with less impact on the coastal current and downstream-located ice shelves. Also, Prince Harald IS, which has a negative melt rate in RJMS, has a large melt rate in the simulations.

Water masses on the continental shelf off Amery IS resemble the cold water ice shelf situation. The overall simulated melt rates of Amery and Publications IS are small and close to observed melt rates. However, the melt rate pattern of Amery deviates from the observed pattern as only small areas contain marine ice formation near the ice front in the simulations. Amery IS has a small positive trend (∼0.1 m/a, both runs) of melt during the integration period, which is opposite to the small negative trend of ∼−0.1 m/a of other ice shelves in this sector. West IS is one of the few ice shelves in the L050 and L100 simulations where an increase of vertical resolution increases the model-data difference in area-averaged melt rate and mass loss.

5.3. Pacific Ocean Sector

The Pacific Sector contains smaller ice shelves with an average RJMS melt rate of 3.7 m/a. The mean modeled melt rate (1.02 m/a in L100) underestimates this considerably (Figure 7 and Table 1) except in the

immediate downstream area of the Ross Sea Sector. This suggests that the influence of the modified water masses of the Western Ross Sea on the coastal current is limited as bathymetric features, i.e., broadening of the shelf and northward guidance of the slope, steer the westward flow. An eastward return flow component becomes apparent near Cape Hudson and Cook IS.

The ice shelves downstream of Cape Adare are either too small (e.g., Dibble and Holmes IS) to be affected by or to impact the coastal current with higher melt rates. Also, the bathymetry might not allow exchanges between subcavity and continental shelf water masses. This means less impact on these ice shelves by additional amounts of freshwater in the coastal current due to upstream ice shelf-ocean interaction.

The L100 melt rates for Totten IS (1.51 m/a) and Moscow University IS (2.80 m/a) are below the RJMS melt rates of 10.5 m/a and 4.7 m/a, respectively. Bathymetry as well as grid spacing are the main causes for the discrepancies. *Khazendar et al*. [2013] needed to adjust the existing near-shore bathymetry for Totten and Moscow University IS in their regional high-resolution model to obtain basal melt rate close to estimates derived from satellite data.

Overall, ice shelves in this sector are comprised by a small number of grid points. Thus, it is not possible to distinguish a spatial variance pattern between ice shelf front and the rest of the cavity. Totten IS, e.g., should have a more refined melt pattern, with large variance at the ice shelf front and little in the deep cavity.

5.4. Ross Sea Sector

The mean basal melt rate (0.51 m/a in L100 and 0.81 m/a in L050) for this sector is in good agreement compared to the RJMS estimates of 0.33 m/a (Figure 7 and Table 1). Next to the large Ross IS in the center of the sector, areas of interest lie to the east and west of Ross IS. The eastern part represents the region with water masses flowing toward the Ross IS. That means that ice shelf-ocean interactions in this part have the potential to influence the melt/freeze behavior of the Ross IS. The western part represents the outflow region whose water masses impact downstream-located ice shelves in the Ross Sea as well as along the continental shelf. The melt rates of ice shelves in the eastern region of the Ross Sea sector (Nickerson and Sulzberger IS) are overestimated compared to RJMS melt rates (Figure 7). The large melt rates result in large basal mass loss and hence a large freshwater input modifying water masses that subsequently enter the Ross IS cavity. This pattern of higher mass loss holds from Getz IS to the eastern Ross Sea sector. Hence, water masses on the thin continental shelf flowing toward the Ross IS are misrepresented. In turn they are the cause for higher modeled melt rates in the eastern part of the Ross IS, the region to the east of Roosevelt Island (Figure 8, right column). The water masses in the eastern part of the cavity are seen as lower salinity and warmer temperatures in the T/S diagram (Figure 10), distinct from the rest of the T/S characteristics of the cavity. The difference between L050 and L100 is small, with L100 being slightly more saline. The temperature of the inflow into the cavity is too warm and is not compensated by a finer resolution at the base of the ice shelf as seen in Filchner IS or Pine Island IS. A higher vertical resolution does not change the properties of the water column enough to better represent the melting in the eastern part of the Ross Sea Sector nor the Ross IS. Finer horizontal grid spacing accompanied with a high number of vertical levels is likely to result in a better representation of the water masses on the continental shelf around Nickerson and Sulzberger IS and along the continental shelf slope, which in turn would result in reduced melting of the eastern Ross IS.

Apart from high melting in the eastern region of the Ross IS, the melt rate and pattern of the central and western Ross IS are in good agreement with observations. Despite the coarse horizontal grid spacing of L050 and L100, a wave like pattern in the central part of the ice shelf seen in RJMS is found in the model results. It reflects the melting due to depth changes at the base of the ice shelf as a result of crevassing

The simulated melt rates in the western region of the Ross Sea Sector are only slightly lower than observed. The mass loss of the ice shelves in this area is small and slightly underestimated, with little fresh water input (Figure 7). The warm temperatures at high salinities (L100, Figure 10c) are found in the deepest part of the western Ross IS cavity, where they remain due to their density.

5.5. Amundsen-Bellingshausen Seas

The Amundsen-Bellingshausen Seas Sector is the most interesting sector to compare model results to observations since the largest observed Antarctic mass loss occurs in this region [*Rignot et al*., 2008, 2013]. Of

particular interest are Pine Island and Thwaites Glaciers, as well as Getz IS, which contribute a large amount of freshwater to the water column and in turn affect downstream-lying ice shelves, e.g., in the Ross Sea Sector.

The model resolution is too coarse to compare melt rate pattern in small ice streams like Pine Island Glacier. Similarly, bathymetric features like the seamount below Pine Island IS shown in *Jenkins et al*. [2010], are not properly resolved.

The melt rates of Pine Island and Getz IS in L050 are larger than observed while that of Thwaites is lower (Figure 7 and Table 1). The increase in vertical layers decreases the melt rate in all three ice shelves. Contrary to Pine Island and Thwaites IS, Getz IS model results are higher, possibly not only due to the coarse horizontal grid spacing but also due to the fact that the shape of the cavity is less well known.

In L050, the vertical temperature section of Pine Island Bay (Figure 11) shows that the pycnocline in the cavity is broad and less defined. Warmer waters enter the cavity leading to higher than observed melting. Thinner levels (L100) in the subice cavities improve the representation of a thin cold layer of water at the base of the ice shelf. This improves the representation of the water column [see *Jenkins et al*., 2010] but reduces the melting to lower than observed values. In L050 the temperatures at the base of the ice shelf are higher by about 0.5°C.

The mean T/S characteristics of the cavities in this sector show little differences between runs, with L100 values on the saltier side (Figure 10). Less melting means less freshwater input into the water column, which leads to a saltier water column.

Melt rates in the Bellingshausen Sea are overestimated in L050 and reduced closer to RJMS in L100, with the exception of Bach IS, which shows the same feature as Larsen and Amery IS, i.e., higher melt rate in L100 than in L050. Stange and Abbot show the same feature as Pine Island IS, i.e., the increase in vertical levels reduces melting to lower than observed values. Wilkins IS melt rates are similar to observations in both simulations.

The largest modeled mass loss is found in Getz and George VI IS (272 $\pm$ 20 Gt/a and 201 $\pm$ 22 Gt/a, respectively, in L100). Getz IS mass loss is larger than observations, possibly because the shape of the cavity in terms of bathymetry and ice shelf thickness is not well known. George VI IS melt rates are higher because of the coarse grid spacing that required an artificial opening of the eastern entrance of the ice shelf needed to allow flow through the cavity.

Not only are George VI melt rates higher compared to observations but L050 rates are almost double compared to L100. The circulation on the continental shelf, which is associated with the inflow of warmer water into the western part of the cavity, is slightly higher in L050 than in L100. This leads to higher melt rates. By way of contrast, the melt behavior of Bach Ice Shelf, which is in the inflow area of this warmer water, shows lower melt rates in L050. The distribution of the vertical levels allows more warm water to enter the Bach cavity in the bottom levels of L100 than in L050. Hence, the lower levels at the entrance of Bach IS are warmer in L100 compared to L050. This increases the melt of Bach IS in L100 and subsequently the outflow of ISW at the base of the ice shelf, setting up an ice pump circulation, which draws warmer water at the bottom and leads to more melt.

6. Causes of Model-Data Differences in Basal Melt

In the previous section, we compared the RJMS estimates of ice shelf basal melt rates and patterns to the L050 and L100 numerical simulations. Both simulations were carried out in a model configuration with 18 km horizontal grid spacing and using the steady state assumption, that is, with time-invariant sub-ice-shelf cavity shape. We find that cold water ice shelves in the Weddell and Ross Seas are reasonably well represented, provided that vertical resolution is sufficient, but warm water ice shelves, like the ones in the Amundsen-Bellingshausen Sea, have large discrepancies relative to observed melt rates. In this section, we discuss some possible causes for these model-data differences.

A principal reason for observed-to-simulated basal melt rate differences is model resolution. With 18 km horizontal grid spacing, the representation of grounding lines and zones in sub-ice-shelf cavities is marginal, that is, the locations of the deepest part of the cavities are displaced relative to their real locations. According to RJMS, the largest melting occurs within 20–30 km of the grounding line, which is

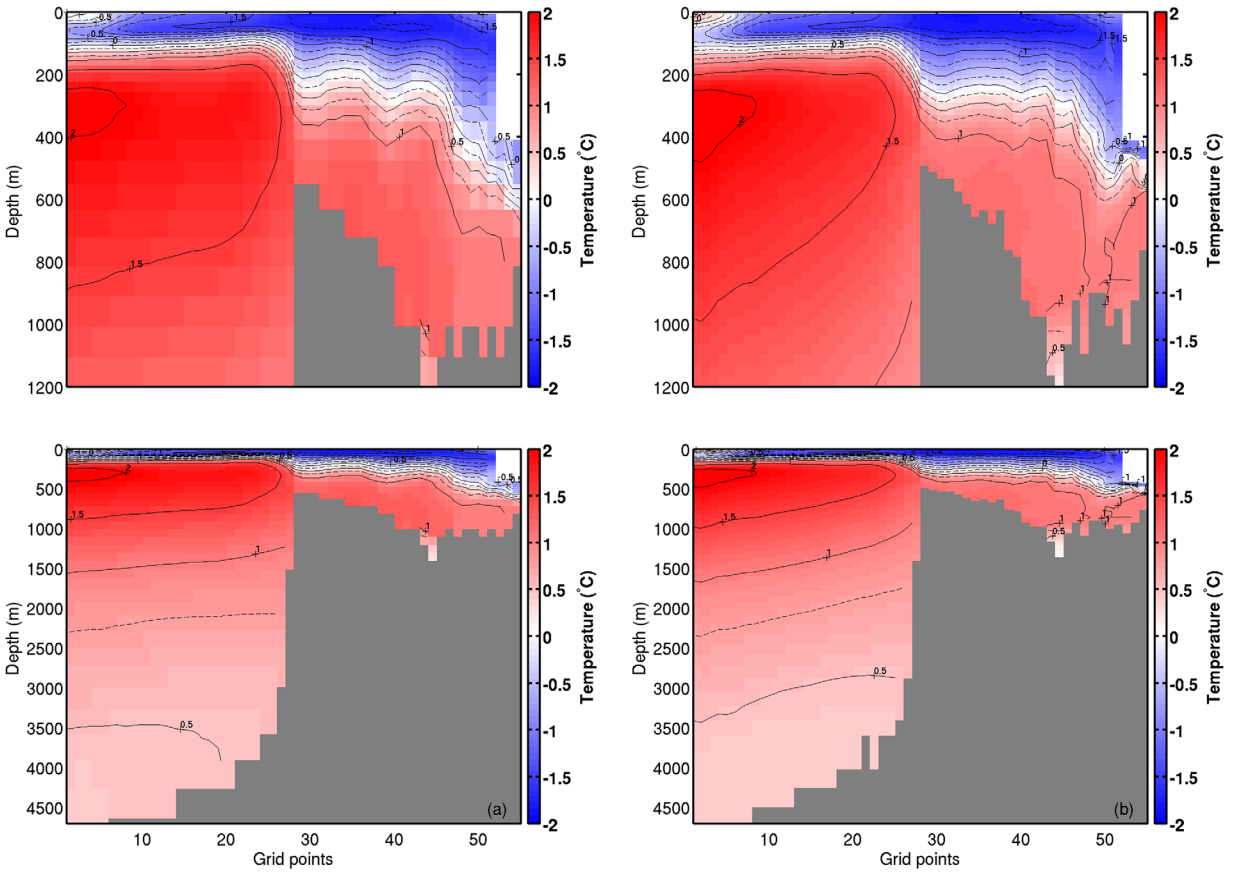

Figure 11. Temperature section of Pine Island Ice Shelf covering the continental shelf as well as part of the deep Amundsen Sea for simulations (a) L050 and (b) L100. Gray shading depicts land and white is ice shelf. Section location is indicated in Figure 2. (top) Top 1200 m and (bottom) the entire water column.

approximately one grid point in our simulations. While high basal melt values are simulated near the grounding line of the Filchner Ronne IS, this is not the case for smaller ice shelves, e.g., the Pine Island IS. This difference is in part caused by the model representation of the troughs where ice streams join ice shelves; while these are reasonably well resolved for the Filchner Ronne IS with an 18 km grid, this is not the case for the smaller ice shelves. Furthermore, bathymetric features, such as seamounts inside the cavity, are smoothed resulting in different circulation patterns and hence in different melt patterns [e.g., *Schodlok et al*., 2012].

Model grid spacing is of importance not only in the sub-ice-shelf cavities but also on the continental shelf. For example, *Schodlok et al*. [2012] showed that an eastern channel on the continental shelf is a main supply route of heat for Pine Island Glacier. In our circumpolar model simulations, the coarse resolution smooths the bathymetry and changes the route of warm waters toward the cavity. Also, the flow of water masses toward the eastern Ross IS is misrepresented regardless of vertical discretization. Warmer than observed waters on the narrow continental shelf are allowed to enter the Eastern Ross IS cavity leading to higher than observed melt rates. Decreasing the horizontal grid spacing would improve the representation of the narrow continental shelves and the structure of the adjacent water masses.

Recent observations, e.g., from Operation IceBridge (OIB), have improved estimates of cavity shapes for the larger ice shelves and for a few smaller ice shelves in the Amundsen-Bellingshausen Seas and the Eastern Weddell Sea. This means that ice shelf-ocean interactions will be better represented in higher-resolution numerical simulations. However, there remain ice shelves, e.g., the Totten IS, for which the most recent state-of-the art bathymetry and ice shelf thickness data used in BEDMAP2 show a negative water column thickness. Modeling ice shelf cavities in these data-poor regions requires guessing the shape of the cavity in

order to allow some water to circulate from the continental shelf to the grounding line. Therefore differences in observed versus simulated basal melt rates are caused not only by poor model resolution but also by lack of accurate bathymetry in the cavities and on the continental shelf.

A source of melt rate errors and uncertainties is the parameterization of turbulent heat and freshwater exchange at the base of the ice shelves. For the 18 km-grid simulations, we used constant heat and freshwater exchange coefficients that do not vary with velocity. For the cold water ice shelf Filchner Ronne IS, this approach not only returns a realistic melt and freezing pattern over the shallow part of the ice shelves, in the vicinity of the Henry and Korff Ice Rises, but also in the deep cavity and in the troughs where the ice streams join the ice shelf. This approach works less well for the smaller, warm water ice shelves, as has been discussed by *Dansereau et al*. [2013].

In general, the warm water ice shelves are smaller in extent and not as deep as the cold water ice shelves. Furthermore, the warm water ice shelves have a stronger transient response that is not captured with the steady-state cavity-shape approach. The shape of the cavity changes with consequences for water masses entering the cavity. For example, the heat exchanged can be controlled by the depth of the thermocline relative to cavity shape [*De Rydt et al*., 2014].

The seasonality of atmosphere-ocean interaction is affected by the rapid retreat of sea ice from winter to spring as discussed in Sect. 4.3. The earlier onset of melt and thus freshwater input in the water column stabilizes the water column with less mixing of colder water to deeper levels. In this way, sea ice formation and retreat affect melting at the ice shelf front edge, where the largest variability was found.

Khazendar et al. [2013] showed that polynya formation is important in modifying water mass properties on the continental shelf, which in turn impacts heat exchange between ocean and ice shelf. The model does not have the capability to simulate land fast ice with consequences for surface ocean circulation and polynya formation. A lack of polynyas and higher sea ice concentration near the coastline results in less atmosphere-ocean interaction and less sea ice formation, which in turn results in less HSSW formation. More heat is available to enter the cavity and contribute to basal melt.

Another source of melt rate errors is the difference between observed and simulated ice shelf areas (Table 1). Although there is no systematic over- or underestimation of the ice shelf area, the 18 km grid spacing does not allow the grounding zone to be accurately represented. In general, a 50% limit of inclusion was applied, i.e., a grid cell is considered ice-shelf-free if it contains less than 50% of the ice shelf. In other instances the ice shelf cavity needs to be artificially increased to allow for observed circulation features. For example, grid cells needed to be added to the northern part of the George VI IS (entrance toward Marguerite Bay) in order to simulate the northward throughflow of water reported by *Jenkins and Jacobs* [2008]. Although this modification allows throughflow to occur, it increases the ice shelf area, resulting in higher integrated melt rates compared to observations. At the southern part George VI IS (Ronne Entrance), the simulated cavity is smaller than observed due to coarseness of model grid and inability to accurately represent the grounding line location.

7. Differences in Simulations With Respect to Number of Vertical Levels

In addition to differences in basal melt rates, simulations L050 and L100 also have substantial differences in water mass properties (see section 4.2). In order to understand these differences, we performed sensitivity experiments with a simplified model configuration. Specifically, we turned off all external forcing (lateral, atmospheric, and sea ice) and prescribed homogeneous initial conditions of -1.9°C and 34.7 salinity. Starting from rest, homogeneous model configurations with 50 (H050) and 100 (H100) vertical levels were integrated for 1 year. The only forcing applied to H050 and H100 is from ice shelf melting and freezing.

Time series of Filchner Ice Shelf area-averaged melt rates for the H050 (gray line) and H100 (black line) simulations are shown in Figure 12a. As expected, the initial melt rate is identical for both H050 and H100, since temperature of water immediately adjacent to the ice is identical for both experiments. As the ice melts, a layer of relatively cold, fresh water forms at the base of the ice shelf, which reduces melt rate. The thinner levels adjacent to the ice in H100 have less heat capacity than those of H050 and hence they cool faster and more. After 1 year of model integration, the melt rate of H100 is approximately half that of H050. This

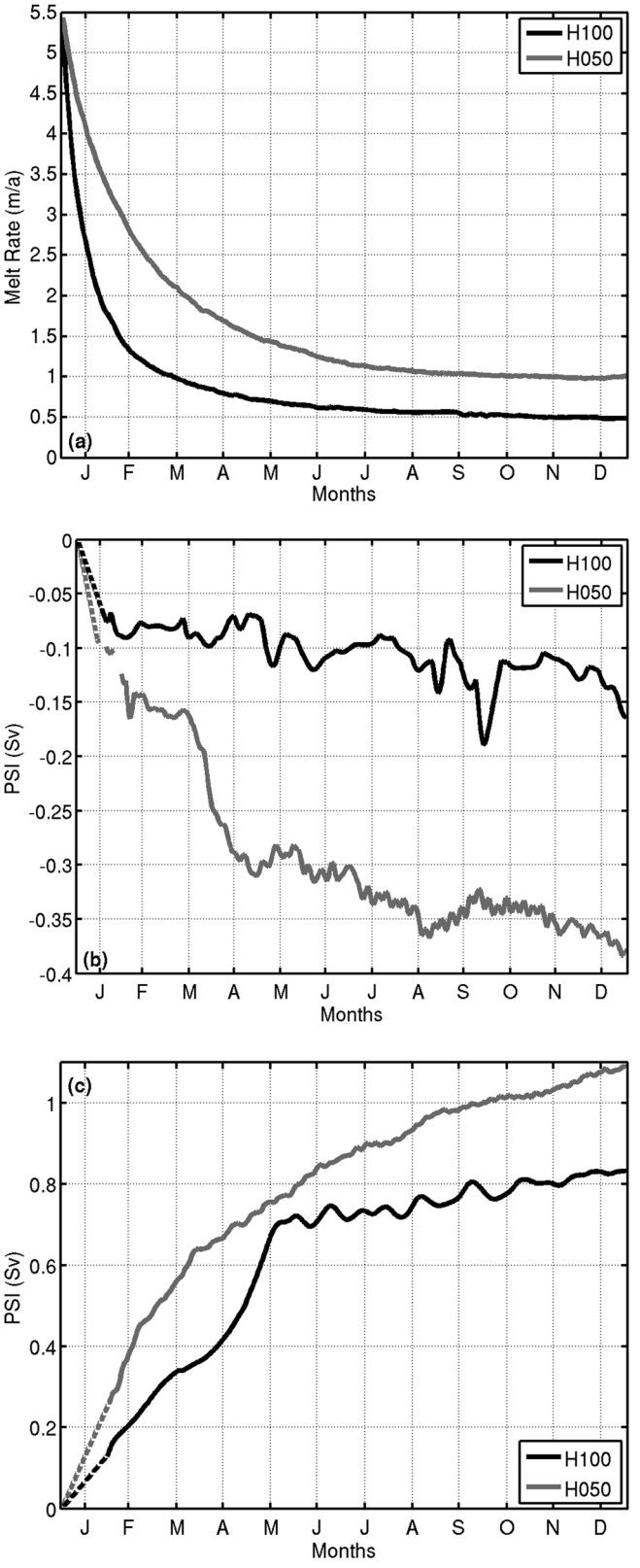

Figure 12. (a) Time series of Filchner Ice Shelf melt rate (m/a),(b) horizontal gyre strength in the Filchner cavity (Sv), and (c) gyre strength over the Filchner Trough just outside the Filchner cavity (Sv) for two sensitivity experiments labeled H050 (gray) and H100 (black). Initialization transients due to sea level adjustment to presence of ice shelf have been removed in Figures 12b and 12c for clarity.

mechanism is also discussed in *Losch* [2008] who find that the thicker the vertical levels in simulated ice shelf cavities, the higher the melt rate.

Although both H050 and H100 are initially at rest, buoyancy forcing from melting water at the base of the ice shelf establishes horizontal gyres and vertical overturning in the two simulations. For example, the two plots of Figure 13 show that relatively strong horizontal circulation patterns are established, up to 1 Sv in magnitude after 1 year of integration, despite the absence of any other forcing apart from basal melt and refreezing. In particular note the anticyclonic gyre (negative contours) under the Filchner Ice Shelf and the cyclonic gyre (positive contours) connecting the edge of the cavity with the warmer waters of the Weddell Gyre. The time evolving strengths of horizontal circulation under and in front of Filchner Ice Shelf are documented on Figures 12b and 12c. In general the larger melt rates of H050 lead to stronger circulation features, by a factor of approximately 2, than in H100. The stronger horizontal gyre circulation of H050 leads to more warm water being transported from the shelf break to the ice shelf cavity, which in turn causes more basal melting. This mechanism explains the warmer water column of L050 versus L100 (Figure 9a versus Figure 9b and the generally larger melt rates of L050 relative to L100. The increased southward heat flux also explains the warmer water column of L050 versus L100 (Figures 9a and 9b) and the generally larger melt rates of L050 relative to L100. For example, the southward heat transport across a section approximately at the edge of the continental shelf in the Southern Weddell Sea increases from 0.5 TW in L100 to 8.3 TW in L050. By comparison surface heating southward of that section by atmosphere and sea ice (−0.6 TW in L100 and 0.2 TW in L050) is an order of magnitude smaller than the 8 TW increase in Southward heat transport.

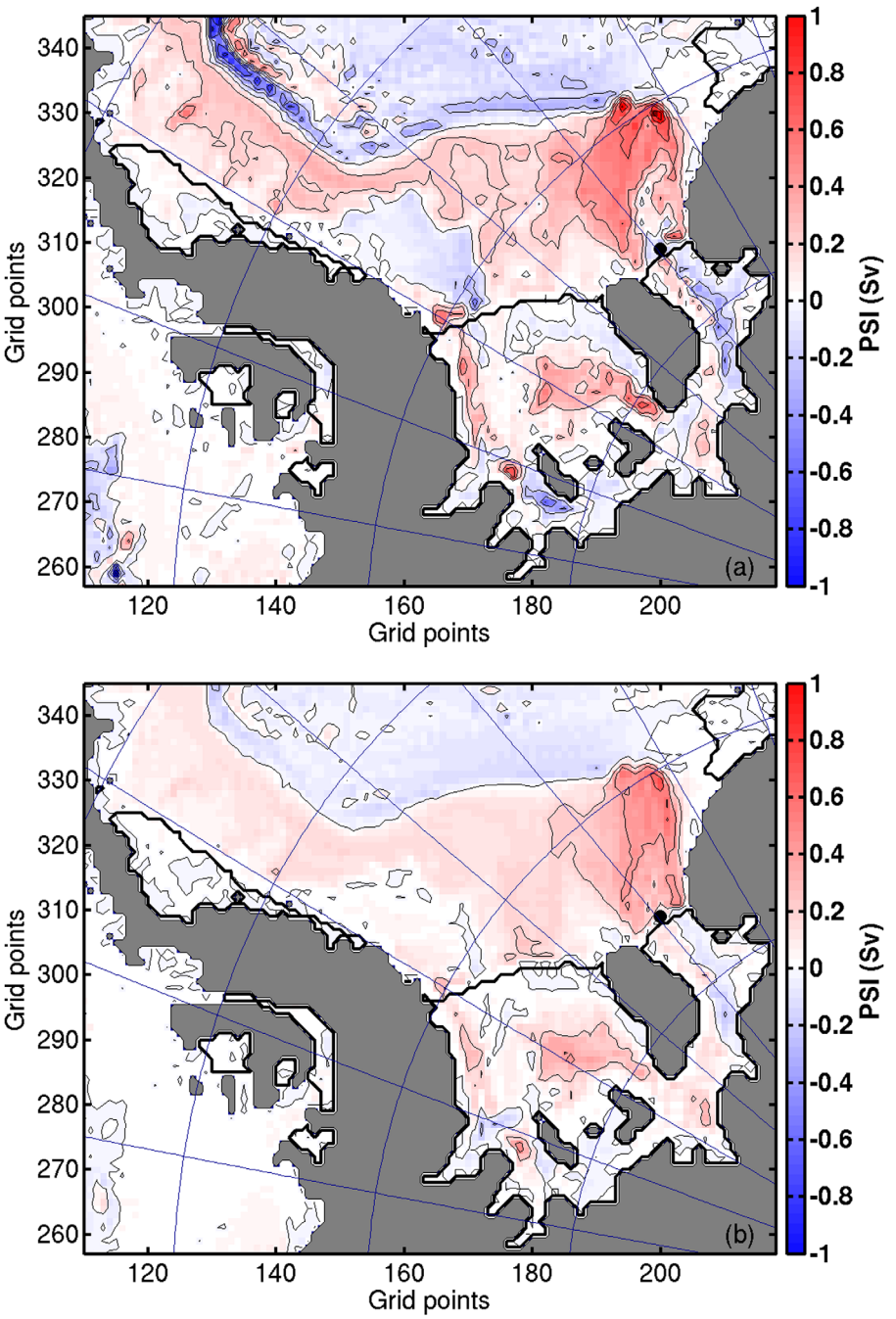

Figure 13. Time mean horizontal stream function (Sv) for the southwestern Weddell Sea for simulations (a) H050 and (b) H100.

8. Summary and Conclusions

We have presented results from the addition of thermodynamic ice shelf cavity physics in a circumpolar Southern Ocean configuration derived from the global ECCO2 model set up of *Menemenlis et al.* [2008]. A first simulation, called L050, resolves 50 ice shelves and glaciers at the Antarctic Continental margin and has the same vertical discretization as the global ECCO2 configuration, that is, 50 vertical levels. The addition of ice shelf cavities in this configuration, keeping all other model parameters unchanged and using the ice shelf melt rate parameterization of *Jenkins et al.* [2001], does not produce melt rates consistent with

observations. For most ice shelves, the L050 simulation overestimates melt rates, which impacts stratification, sea ice formation, and circulation. The overestimation of ice shelf melt rates cools and freshens the water column, inhibits bottom water mass formation, allows warmer circumpolar waters to enter the central Weddell Sea, and erodes all preexisting Weddell Sea Bottom Water. This leads to, e.g., an overestimation of Filchner IS melting, with a mean mass loss of 534 ± 40 Gt/a in L050 versus 41.9 ± 10 Gt/a in the *Rignot et al.* [2013] observations.

In a second simulation, called L100, we increased the number of vertical levels to 100, leading to $\Delta z \leq 30$ m in the sub-ice-shelf cavities and improved resolution of the continental shelf depth range. Thinner levels in the sub-ice-shelf cavities improve the representation of a thin, cold-water layer at the ice shelf base, thus leading to a better representation of the T/S characteristics of the water column. Thinner levels at the continental shelf depth range lead to improved representation of open-ocean to continental-shelf exchanges. This leads to to time-mean basal melt rates and patterns that are in closer agreement with the *Rignot et al.* [2013] observations and to improved representation of ocean circulation within and outside the cavities and of open-ocean to continental-shelf exchanges. In particular, the melt/freezing areas of large, cold water ice shelves (Filchner-Ronne, Ross, and Amery) are well captured. In the case of Filchner Ronne, the L100 reduction of melt water input, compared to L050, leads to a warmer water column downstream near Larsen IS, which now shows higher melt rates closer to observations.

The largest differences relative to observations occur under warm water ice shelves in the Amundsen-Bellingshausen Sea, where the majority of mass loss is reported to occur [*Rignot et al.*, 2008, 2013]. While L100 melt rates are lower than L050, they are still too high compared to observations. The crude representation of the shape of the cavity on an 18 km grid and errors in the model's representation of continental shelf water masses are the primary causes for a higher heat delivery to the warm-water ice shelves, thus higher melt rates. Other sources of errors are the simplified parameterization of the turbulent exchange and uncertainties in the, possibly time evolving, shape of the sub-ice-shelf cavities

This study demonstrates that the explicit representation of thermodynamic ice-shelf cavities in ocean retrospective analyses and ocean climate models that have horizontal grid spacing of 20 km or less can lead to realistic representation of time-mean basal melt rates and patterns for the large cold water ice shelves (Filchner-Ronne, Ross, and Amery), provided that vertical grid spacing is sufficiently small to resolve sub-ice-shelf stratification. The explicit representation of thermodynamic ice-shelf cavities is a key requirement for ocean climate analyses and simulations that aim to understand impact of time-evolving ice-shelf basal melt rates on Antarctic ice sheets and global ocean circulation. Further improvements to the representation of ice shelf-ocean interactions at this horizontal resolution ($\sim$20 km grid spacing) are expected to follow from spatially varying time-independent adjustment of the model's subgrid-scale parameterizations, e.g., ice-shelf turbulent exchange coefficients, sea-ice and salt plume parameters, bottom boundary layer transport and entrainment parameters, vertical diffusivity, and the *Redi* [1982] and *Gent and McWilliams* [1990] coefficients. These improved subgrid-scale parameterizations can be informed by high-resolution regional studies [e.g., *Schodlok et al.*, 2012; *Khazendar et al.*, 2013] or coarse-resolution parameter optimization studies, e.g., using adjoint [*Heimbach and Losch*, 2012] or Green's function [*Nguyen et al.*, 2011] methods.

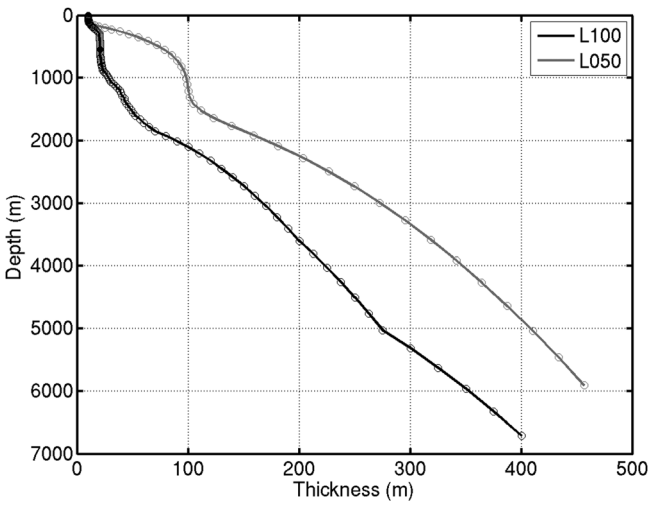

Figure A1. Depths (m) vs thickness (m) of vertical levels for runs L050 and L100.

Appendix A

Figure A1 shows thickness of vertical levels versus depth for the L050 and L100 model configurations.

Table A1. Water Mass Characteristics of the Weddell Sea in Θ/S Space

Watermass		Θ (°C)	Salinity
Warm Deep Water	WDW	0.0–0.6	34.6–34.75
Low Salinity Shelf Water	LSSW	−1.9 to−1.5	34.3–34.35
High Salinity Shelf Water	HSSW	−2.0 to−1.5	34.55–34.85
Weddell Sea Deep Water	WSDW	−0.7 to 0.0	34.64–34.70
Weddell Sea Bottom Water	WSBW	−1.5 to−0.7	> 34.55
Ice Shelf Water	ISW	< −1.9	34.56–34.70

The major difference is seen in the top 2000 m, with finer spacing in L100. The thickness of L100 levels does not exceed 30 m in the top 1000 m.

Weddell Sea water mass definitions and characteristicsm, as used in section 4, are listed in Table A1.

Acknowledgments

This research was carried out, in part, at the Jet Propulsion Laboratory, California Institute of Technology, under a contract with the National Aeronautics and Space Administration (NASA). We gratefully acknowledge support from the NASA Modeling, Analysis, and Prediction (MAP) and Cryospheric Sciences Programs. Computational resources were provided by the NASA Advanced Supercomputing (NAS) Division. This work is a contribution to the ECCO-IcES project and to University of California, Irvine NASA grant NNX13AN46G. We thank C. Rodehacke and M. Flexas for helpful comments and discussions to improve the manuscript. Model input data are available on http://ecco2.jpl.nasa.gov/products and model output by contacting M.P. Schodlok.

References

Adcroft, A., C. Hill, and J. Marshall (1997), *The representation of topography by shaved cells in a height coordinate model, Mon. Weather Rev.*, *125*(9), 2293–2315.

Antonov, J. I., et al. (2010), *World Ocean Atlas 209, Volume 2: Salinity*, U.S. Gov. Print. Off., Washington, D. C.

Arndt, J. E., et al. (2013), The International Bathymetric Chart of the Southern Ocean (IBCSO) Version 1.0––A new bathymetric compilation covering circum-Antarctic waters, *Geophys. Res. Lett.*, *40*, 3111–3117, doi:10.1002/grl.50413.

Assmann, K., and R. Timmermann (2005), Variability of dense water formation in the Ross Sea, *Ocean Dyn.*, *55*, 68–87, doi:10.1007/s10236-004-0106-7.

Beckmann, A., and R. Timmermann (2001), Circumpolar influences on the Weddell Sea: Indication of an Antarctic circumpolar coastal wave, *J. Oceanogr.*, *14*(17), 3785–3792.

Beckmann, A., H. Hellmer, and R. Timmermann (1999), A numerical model of the Weddell Sea: Large-scale circulation and water mass distribution, *J. Geophys. Res.*, *104*(23), 23,375–23,391.

Dansereau, V., P. Heimbach, and M. Losch (2013), Simulation of subice shelf melt rates in a general circulation model: Velocity-dependent transfer and the role of friction, *J. Geophys. Res. Oceans*, *119*, 1765–1790, doi:10.1002/2013JC008846.

Daru, V., and C. Tenaud (2004), High order one-step monotonicity-preserving schemes for unsteady compressible flow calculations, *J. Comput. Phys.*, *193*, 563–594.

De Rydt, J., P. Holland, P. Dutrieux, and A. Jenkins (2014), Geometric and oceanographic controls on melting beneath pine island glacier, *J. Geophys. Res. Oceans*, *119*, 2420–2438, doi:10.1002/2013JC009513.

Dinniman, M. S., J. M. Klinck, and E. E. Hofmann (2012), Sensitivity of circumpolar deep water transport and ice shelf basal melt along the west Antarctic Peninsula to changes in the winds, *J. Oceanogr.*, *25*, 4799–4816, doi:10.1175/JCLI-D-11-00307.1.

Dotto, T. S., R. Kerr, M. M. Mata, M. Azaneu, I. Wainer, E. Fahrbach, and G. Rohardt (2014), Assessment of the structure and variability of Weddell Sea water masses in distinct ocean reanalysis products, *Ocean Sci.*, 523–546 doi:10.5194/os-10-523-2014.

Fahrbach, E., G. Rohardt, M. Schröder, and V. H. Strass (1994), Transport and structure of the Weddell Gyre, *Ann. Geophys.*, *12*(9), 840, doi:10.1007/s005850050109.

Firing, Y., T. K. Chereskin, and M. R. Mazloff (2011), Vertical structure and transport of the Antarctic circumpolar current in drake passage from direct velocity observations, *J. Geophys. Res.*, *116*, C08015, doi:10.1029/2011JC006999.

Foldvik, A., T. Gammelsrød, and T. Tørresen (1985), Circulation and water masses on the southern Weddell Sea shelf, in *Oceanology of the Antarctic Continental Shelf*, vol. 43, edited by S. S. Jacobs, pp. 5–20, AGU, Washington, D. C.

Fox-Kemper, B., and D. Menemenlis (2008), Can large eddy simulation techniques improve mesoscale rich ocean models?, in *Ocean Modeling in an Eddying Regime*, edited by M. Hecht and H. Hasumi, pp. 319–388, AGU, Washington, D. C.

Fretwell, P. T., et al. (2013), Bedmap2: Improved ice bed, surface and thickness datasets for Antarctica, *Cryosphere*, *7*(1), 375–393, doi:10.5194/tc-7-375-2013.

Gent, P., and J. McWilliams (1990), Isopycnal mixing in ocean circulation models, *J. Phys. Oceanogr.*, *20*, 150–155.

Gille, S. T. (2002), Warming of the southern ocean since the 1950s, *Science*, *295*(5558), 1275–1277, doi:10.1126/science.1065863.

Griggs, J. A., and J. L. Bamber (2011), Antarctic ice-shelf thickness from satellite radar altimetry, *J. Glaciol.*, *57*(203), 485–498, doi:10.3189/002214311796905659.

Grosfeld, K., M. Schröder, E. Fahrbach, R. Gerdes, and A. Mackensen (2001), How iceberg calving and grounding change the circulation and hydrography in the Filchner Ice Shelf Ocean System, *J. Geophys. Res.*, *106*(C5), 9039–9055.

Haran, T., J. Bohlander, and M. Fahnestock (2005), *Modis Mosaic of Antarctica (MOA) Image Map*, Natl. Snow and Ice Data Cent., Boulder, Colo.

Hattermann, T., O. Nøst, J. Lilly, and L. Smedsrud (2012), Two years of oceanic observations below the Fimbul Ice Shelf, Antarctica, *Geophys. Res. Lett.*, *39*, L12605, doi:10.1029/2012GL051012.

Heimbach, P., and M. Losch (2012), Adjoint sensitivities of sub-ice shelf melt rates to ocean circulation under Pine Island Ice Shelf, West Antarctica, *Ann. Glaciol.*, *53*, 60A025.

Hellmer, H. (2004), Impact of Antarctic ice shelf basal melting on sea ice and deep ocean properties, *Geophys. Res. Lett.*, *31*, L10307, doi:10.1029/2004GL019506.

Hellmer, H., and D. Olbers (1989), A two-dimensional model of the thermohaline circulation under an ice shelf, *Antarct. Sci.*, *1*(4), 325–336.

Hellmer, H. H., M. P. Schodlok, M. Wenzel, and J. G. Schröter (2005), On the influence of adequate Weddell Sea characteristics in a large-scale global ocean circulation model, *Ocean Dyn.*, *55*(2), 88–99, doi:10.1007/s10236-005-0112-4.

Holland, D., and A. Jenkins (1999), Modelling thermodynamic ice-ocean interactions at the base of an ice shelf, *J. Phys. Oceanogr.*, *29*(8), 1787–1800.

Holland, P. R., A. Jenkins, and D. M. Holland (2010), Ice and ocean processes in the Bellingshausen Sea, Antarctica, *J. Geophys. Res.*, *115*, C05020, doi:10.1029/2008JC005219.

Jacobs, S., H. Hellmer, C. Doake, A. Jenkins, and R. Frolich (1992), Melting of ice shelves and the mass balance of Antarctica, *J. Glaciol.*, *38*(130), 375–387.

Jacobs, S. S. (2006), Observations of change in the Southern Ocean, *Philos. Trans. R. Soc. A*, *364*(1844), 1657–1681, doi:10.1098/rsta.2006.1794.

Jacobs, S. S., A. Jenkins, C. F. Giulivi, and P. Dutrieux (2011), Stronger ocean circulation and increased melting under Pine Island Glacier ice shelf, *Nat. Geosci.*, *4*(8), 519–523, doi:10.1038/ngeo1188.

Jansen, D., M. P. Schodlok, and W. Rack (2007), Basal melting of A-38B: A physical model constrained by satellite observations, *Remote Sens. Environ.*, *111*(2-3), 195–203, doi:10.1016/j.rse.2007.03.022.

Jenkins, A., and S. Jacobs (2008), Circulation and melting beneath George VI ice shelf, Antarctica, *J. Geophys. Res.*, *113*, C04013, doi:10.1029/2007JC004449.
Jenkins, A., H. Hellmer, and D. Holland (2001), The role of meltwater advection in the formulation of conservative boundary conditions at an ice-ocean interface, *J. Phys. Oceanogr.*, *31*(1), 285–296.
Jenkins, A., P. Dutrieux, S. Jacobs, S. McPhail, J. Perrett, A. Webb, and D. White (2010), Observations beneath Pine Island Glacier in West Antarctica and implications for its retreat, *Nat. Geosci.*, *3*(7), 468–472, doi:10.1038/ngeo890.
Joughin, I., and L. Padman (2003), Melting and freezing beneath Filchner-Ronne Ice Shelf, Antarctica, *Geophys. Res. Lett.*, *30*(9), 1477, doi:10.1029/2003GL016941.
Khazendar, A., M. Schodlok, I. Fenty, S. Ligtenberg, E. J. Rignot, and M. van den Broeke (2013), Observed thinning of Totten Glacier is linked to coastal polynya variability, *Nat. Commun.*, *4*, 2857, doi:10.1038/ncomms3857.
Klatt, O., E. Fahrbach, M. Hoppema, and G. Rohardt (2005), The transport of the Weddell Gyre across the Prime Meridian, *Deep Sea Res., Part II*, *52*(3-4), 513–528, doi:10.1016/j.dsr2.2004.12.015.
Large, W., J. C. McWilliams, and S. Doney (1994), Oceanic vertical mixing: A review and a model with a nonlocal boundary layer parameterization, *Rev. Geophys.*, *32*(4), 363–403.
Locarnini, R., et al. (2010), *World Ocean Atlas 2009, Volume 1: Temperature*, U.S. Gov. Print. Off., Washington, D. C.
Loose, B., P. Schlosser, W. Smethie, and S. Jacobs (2009), An optimized estimate of glacial melt from the ross ice shelf using nobel gases, stable isotopes, and cfc transient tracers, *J. Geophys. Res.*, *114*, C08007, doi:10.1029/2008JC005048.
Losch, M. (2008), Modeling ice shelf cavities in a z coordinate ocean general circulation model, *J. Geophys. Res.*, *113*, C08043, doi:10.1029/2007JC004368.
Losch, M., D. Menemenlis, J.-M. Campin, P. Heimbach, and C. Hill (2010), On the formulation of sea-ice models. Part 1: Effects of different solver implementations and parameterizations, *Ocean Modell.*, *33*(1–2), 129–144.
Marshall, J., A. Adcroft, C. Hill, L. Perelman, and C. Heisey (1997), A finite-volume, incompressible Navier-Stokes model for studies of the ocean on parallel computers, *J. Geophys. Res.*, *102*(C3), 5753–5766.
Menemenlis, D., J.-M. Campin, P. Heimbach, C. Hill, T. Lee, A. Nguyen, M. Schodlok, and H. Zhang (2008), ECCO2: High resolution global ocean and sea ice data synthesis, *Mercator Ocean Q. Newsl.*, *31*, 13–21.
Mosby, H. (1934), The waters of the Atlantic Antarctic Ocean, *Det Norske Viden. Akad., Sci. Res. Norw. Antarct. Exped.*, 1927–1928, *1*(11), 131 pp.
Nguyen, A. T., D. Menemenlis, and R. Kwok (2011), Arctic ice-ocean simulation with optimized model parameters: Approach and assessment, *J. Geophys. Res.*, *116*, C04025, doi:10.1029/2010JC006573.
Nicholls, K. (2004), Interannual variability and ventilation timescales in the ocean cavity beneath Filchner-Ronne Ice Shelf, Antarctica, *J. Geophys. Res.*, *109*, C04014, doi:10.1029/2003JC002149.
Nicholls, K., S. Østerhus, K. Makinson, and M. Johnson (2001), Oceanographic conditions south of Berkner island, beneath Filchner-Ronne ice shelf, Antarctica, *J. Geophys. Res.*, *106*(6), 11,481–11,492, doi:10.1029/2000JC000350.
Nicholls, K., L. Padman, M. Schröder, R. Woodgate, A. Jenkins, and S. Østerhus (2003), Water mass modification over the continental shelf north of Ronne Ice Shelf, Antarctica, *J. Geophys. Res.*, *108*(8), 3260, doi:10.1029/2002JC001713.
Nicholls, K., et al. (2006), Measurements beneath an Antarctic ice shelf using an autonomous underwater vehicle, *Geophys. Res. Lett.*, *33*, L08612, doi:10.1029/2006GL025998.
Onogi, K., et al. (2007), The jra-25 reanalysis, *J. Meteorol. Soc. Jpn.*, *85*, 369–432.
Paolo, F., H. Fricker, and L. Padman (2015), Volume loss from Antarctic ice shelves is accelerating, *Science*, *348*(6232), 327–331, doi:10.1126/science.aaa0940.
Redi, M. (1982), Oceanic isopycnal mixing by coordinate rotation, *J. Phys. Oceanogr.*, *12*, 1154–1158.
Rignot, E., J. Bamber, M. V. D. Broeke, C. Davis, Y. Li, W. J. V. D. Berg, and E. van Meijgaard (2008), Recent Antarctic ice mass loss from radar interferometry and regional climate modelling, *Nat. Geosci.*, *1*, 106–110.
Rignot, E., J. Mouginot, and B. Scheuchl (2011), Antarctic grounding line mapping from different satellite radar interferometry, *Geophys. Res. Lett.*, *38*, L10504, doi:10.1029/2011GL047109.
Rignot, E., S. Jacobs, J. Mouginot, and B. Scheuchl (2013), Ice shelf melting around Antarctica, *Science*, *314*(6143), 266–270 doi:10.1126/science.1235798.
Schmidtko, S., K. Heywood, A. Thompson, and S. Aoki (2014), Multidecadal warming of Antarctic waters, *Science*, *346*(6214), 1227–1231, doi:10.1126/science.1256117.
Schodlok, M., H. Hellmer, G. Rohardt, and E. Fahrbach (2006), Weddell Sea iceberg drift: Five years of observations, *J. Geophys. Res.*, *111*, C06018, doi:10.1029/2004JC002661.
Schodlok, M., M. Wenzel, J. G. Schröter, and H. H. Hellmer (2008), Regional and global effects of southern ocean constraints in a global model, *Ocean Dyn.*, *58*, 155–168, doi:10.1007/s10236-008-0143-8.
Schodlok, M., D. Menemenlis, E. Rignot, and M. Studinger (2012), Sensitivity of the ice-shelf/ocean system to the sub-ice-shelf cavity shape measured by NASA IceBridge in pine island glacier, west Antarctica, *Ann. Glaciol.*, *53*(60), 156–162, doi:10.3189/2012AoG60A073.
Schröder, M., and E. Fahrbach (1999), On the structure and the transport of the eastern Weddell Gyre, *Deep Sea Res., Part II*, *46*, 501–527.
Smedsrud, L. H. (2005), Warming of the deep water in the Weddell Sea along the Greenwich Meridian: 1977-2001, *Deep Sea Res., Part I*, *52*, 241–258, doi:10.1016/j.dsr.2004.10.004.
Smith, K. L., B. H. Robison, J. J. Helly, R. S. Kaufmann, H. A. Ruhl, T. J. Shaw, B. S. Twining, and M. Vernet (2007), Free-drifting icebergs: Hot spots of chemical and biological enrichment in the Weddell Sea, *Science*, *317*(5837), 478–82, doi:10.1126/science.1142834.
Smith, W. H. F., and D. T. Sandwell (1997), Global sea floor topography from satellite altimetry and ship depth soundings, *Science*, *277*, 1957–1962.
Stanton, T. P., W. J. Shaw, M. Truffer, H. F. J. Corr, L. E. Peters, K. L. Riverman, R. Bindschadler, D. M. Holland, and S. Anandakrishnan (2013), Channelized ice melting in the ocean boundary layer beneath pine island glacier, Antarctica, *Science*, *341*, 1236–1239, doi:10.1126/science.1239373.
Stocker, T. F., D. Qin, G.-K. Plattner, M. Tignor, S. K. Allen, J. Boschung, A. Nauels, Y. Xia, V. Bex, and P. Midgley (Eds.) (2013), *Climate Change 2013: The Physical Science Basis. Contribution of Working Group I to the Fifth Assessment Report of the Intergovernmental Panel on Climate Change*, 1535 pp., Cambridge Univ. Press, N. Y.
Thomas, R., and C. Bentley (1978), A model for Holocene retreat of the west Antarctic ice sheet, *Quat. Res.*, *10*, 150–270.
Timmermann, R., A. Beckmann, and H. H. Hellmer (2002), Simulations of ice-ocean dynamics in the Weddell Sea 1. Model configuration and validation, *J. Geophys. Res.*, *107*(C3), 3024, doi:10.1029/2000JC000741.
Timmermann, R., Q. Wang, and H. H. Hellmer (2012), Ice-shelf basal melting in a global finite-element sea-ice/ice-shelf/ocean model, *Ann. Glaciol.*, *53*(60), 303–314. doi:10.3189/2012AoG60A156.

Whitworth, T., III (1983), Monitoring the transport of the Antarctic Circumpolar Current at Drake Passage, *J. Phys. Oceanogr.*, *13*, 2045–2057.
Whitworth, T., III, and R. G. Peterson (1985), Volume transport of the Antarctic Circumpolar Current from bottom pressure measurements, *J. Phys. Oceanogr.*, *15*, 810–816.
Wunsch, C., and P. Heimbach (2013), Dynamically and kinematically consistent global ocean circulation and ice state estimates, in *Ocean Circulation and Climate: A 21st Century Perspective*, edited by J. G. Gerold Siedler, S. M. Griffies, and J. A. Church, chap. 21, pp. 553–579, Academic, N. Y.
Xue, Y., M. A. Balmaseda, T. Boyer, N. Ferry, S. Good, I. Ishikawa, A. Kumar, M. Rienecker, A. J. Rosati, and Y. Yin (2012), A comparative analysis of upper-ocean heat content variability from an ensemble of operational ocean reanalyses, *J. Clim.*, *25*, 6905–6929.
Zwally, H., J. Comiso, C. Parkinson, D. Cavalieri, and P. Gloersen (2002), Variability of Antarctic sea ice 1979-1998, *J. Geophys. Res.*, *107*(C5), 3041, doi:10.1029/2000JC000733.